INL/EXT-20-59392 Rev. 0

BISON Capabilities for LWR Fuel Behavior Analysis During Accident and High-burnup Conditions

July 2020

M2 Technical Report

Aysenur Toptan[1], Kyle A. Gamble[1], and Giovanni Pastore[1,2]

[1]Idaho National Laboratory
[2]University of Tennessee, Knoxville

Changing the World's Energy Future

Idaho National Laboratory

INL is a U.S. Department of Energy National Laboratory operated by Battelle Energy Alliance, LLC

BISON Capabilities for LWR Fuel Behavior Analysis During Accident and High-burnup Conditions

M2 Technical Report

Aysenur Toptan[1], Kyle A. Gamble[1], and Giovanni Pastore[1,2]

[1]Idaho National Laboratory
[2]University of Tennessee, Knoxville

July 2020

Idaho National Laboratory
Computational Mechanics and Materials Department
Idaho Falls, Idaho 83415

http://www.inl.gov

Prepared for the
U.S. Department of Energy
Office of Nuclear Energy
Under U.S. Department of Energy-Idaho Operations Office
Contract DE-AC07-05ID14517

Page intentionally left blank

Abstract

The U.S. Department of Energy (DOE)'s Nuclear Energy Advanced Modeling and Simulation (NEAMS) program aims to develop predictive capabilities using computational methods for the analysis and design of advanced reactor and fuel cycle systems. This program has been supporting the development of BISON, a high-fidelity and high-resolution fuel performance tool at the engineering scale.

Recent increasing interest in applications at extended burnups motivated this study to incorporate more physically based models in BISON. This document details integration of newly implemented modeling capabilities for BISON. These include: (1) new thermal conductivity models that are valid up to 100 GWd/t, (2) models for the formation of the high-burnup structure (HBS), (3) two porosity correction methods applied to the thermal conductivity due to the conducting pores during the HBS formation. BISON's results are verified and validated to test the new modeling capabilities.

Page intentionally left blank

Acknowledgments

The submitted manuscript has been authored by a contractor of the U.S. Government under Contract DE-AC07-05ID14517. Accordingly, the U.S. Government retains a non-exclusive, royalty-free license to publish or reproduce the published form of this contribution, or allow others to do so, for U.S. Government purposes.

This research made use of the resources of the High Performance Computing Center at Idaho National Laboratory, which is supported by the Office of Nuclear Energy of the U.S. Department of Energy and the Nuclear Science User Facilities under Contract No. DE-AC07-05ID14517.

Page intentionally left blank

Contents

List of Figures

List of Tables

List of Symbols

Greek Letters

α	volume fraction of the new phase	
ϵ	observed error	
γ	Avrami constant	
μ	mean	
σ	standard deviation	
$\boldsymbol{\theta}$	coefficient matrix	
$\boldsymbol{v}$	observations	

Roman Letters

Bu	burnup	MWd/kgU
gd	gadolinia concentration	
H	Heaviside step function	
h	mesh size	
K	transformation rate constant	
k	thermal conductivity	$\mathrm{W/m-K}$
p	porosity or observed order-of-accuracy	
r	radius or mesh refinement factor	
T	temperature	K
t	time	

Subscripts

ann	annealing
eff	effective
i	inner
irr	irradiation
m	maximum
o	outer

Acronyms

DOE	U.S. Department of Energy
DRAM	delayed rejection adaptive Metropolis
EOL	end of life
FE	finite element
FEM	finite element method
FGR	fission gas release
FUMAC	Fuel Modelling in Accident Conditions
HBS	high-burnup structure
HIGB	high-angle grain boundaries
INL	Idaho National Laboratory
KJMA	Kolmogorov-Johnson-Mehl-Avrami
LAGB	low-angle grain boundaries
LOCA	loss of coolant accident
LTE	linear truncation error
LWR	light water reactor
MCMC	Markov Chain Monte Carlo
MES	method of exact solutions
MOOSE	Multiphysics Object-Oriented Simulation Environment
NEAMS	Nuclear Energy Advanced Modeling and Simulation
PIE	post-irradiation examination
PWR	pressurized water reactor
TD	theoretical density
TRISO	tri-structural isotropic

1. Introduction

The U.S. Department of Energy (DOE)'s Nuclear Energy Advanced Modeling and Simulation (NEAMS) program aims to develop predictive capabilities using computational methods for the analysis and design of advanced reactor and fuel cycle systems. The NEAMS program has been supporting the development of BISON which is used as the high-fidelity and high-resolution fuel performance tool at the engineering scale.

BISON [1, 2, 3] is a fuel performance code which models the thermo-mechanical behavior of nuclear fuel using high-performance modeling and simulation. BISON is established on the Multiphysics Object-Oriented Simulation Environment (MOOSE) framework[1] [4, 5] of Idaho National Laboratory (INL). BISON solves the fully-coupled equations of energy conservation, mechanics, and species conservation to account for a large range of fuel behaviors. It is capable of modeling traditional light water reactor (LWR) fuel rods, fuel plates, and tri-structural isotropic (TRISO) fuel particles [6, 7]. It can employ three-dimensional Cartesian, two-dimensional axisymmetric, two-dimensional generalized plane strain, layered two-dimensional, layered one-dimensional, and one-dimensional radial spherical geometries. It includes empirical models for a large variety of fuel thermal and mechanical physics.

Increasing recent interest in applications at extended burnups ($\geq 60\,\mathrm{MWd/kgU}$) motivated this work. In particular, we focus on thermal conductivity modeling for LWR fuel rods in engineering-scale applications. Occurrence of the high-burnup structure (HBS) formation in a range of 60–80 MWd/kgU [8, 9, 10, 11, 12] impacts the thermal conductivity. Our goal is to enhance BISON's modeling capabilities for HBS by adding new thermal conductivity models that are valid up to 100 GWd/t, HBS formation models, and porosity correction methods applied on thermal conductivity for the conducting pores during the HBS formation. These models provide an improved prediction of the fuel behavior at extended burnups. As utilities push to increase the regulatory discharge burnup limit from 62 MWd/kgU to 68 MWd/kgU and beyond, advanced modeling and simulation tools are necessary for understanding fuel rod behavior during both normal operation and design-basis accidents (e.g., loss of coolant accident (LOCA)).

This study focuses on expanding the HBS capabilities of BISON during accident and high-burnup conditions. The new code capabilities are outlined in Chapter 2. They include thermal conductivity models at the extended burnups, models to better predict the behavior during HBS formation, and correction methods on the thermal conductivity of conducting pores due to the HBS formation. To ensure that the code functions correctly and is reliable, a verification study is performed in Chapter 3. To assess the code predictions with

[1] a high-performance, open source, C++ finite element (FE) framework: `www.github.com/idaholab/moose`

the new modeling capabilities against the actual behavior of real-world systems, the code predictions are compared to experiments in Chapter 4. The document concludes with a discussion of the results and future work in Chapter 5. Lastly, the publications documenting BISON's accident capability prior to the addition of the latest models described within this report are highlighted in Chapter 6.

2. New BISON Capabilities

This chapter introduces BISON's new modeling capabilities to compute the thermal conductivity at extended burnups and to accurately model the fuel behavior during the formation of high-burnup structure (HBS). Section 2.1 outlines the newly implemented thermal conductivity models. The models are applicable to uranium dioxide and Gd-bearing uranium dioxide fuels and are valid up to 100 GWd/t. Section 2.2 describes a model to compute the evolution of the local volume fraction of restructured (HBS) fuel considering the progressive formation of the HBS with increasing local burnup in addition to the temperature-dependence of the restructuring process. The restructured (HBS) fuel results in a more porous material. Section 2.3 describes a surrogate model for the porosity formation as a function of local burnup. The resulting porous material will consequentially impact the fuel thermal conductivity because of the gas-filled conducting pores. Section 2.4 provides the newly implemented correction methods on the thermal conductivity model for the conducting pores.

2.1 Thermal Conductivity Models

Ronchi et al. [13] and Staicu et al. [14] combine the effects of burnup, irradiation, and post-irradiation temperature histories in formulating a thermal conductivity model of UO_2, which is considered to be valid up to 100 MWd/kg$_U$. The thermal conductivity, k (W/m-K) at 95% theoretical density (TD) (i.e., normalized to 5 vol.% as-fabricated porosity) is given by, as a summation of the phonon-phonon interaction term, k_{phonon} by [13, 14] and the electronic term, $k_{electronic}$ by [15], in the following form:

$$k_{95} = k_{phonon} + k_{electronic} \tag{2.1a}$$

$$k_{phonon} = \frac{1}{A(T_{irr}, T_{ann}, bu) + B(T_{irr}, T_{ann}, bu)T} \tag{2.1b}$$

$$k_{electronic} = \frac{6400}{t_n^{2.5}} \exp\left(-\frac{16.35}{t_n}\right) \tag{2.1c}$$

where bu is the burnup (GWd/t), T_{irr} is the irradiation temperature (K), T_{ann} is the maximum temperature reached during out-of-pile annealing (K), T is the instant application temperature (K), and $t_n = T/1000$ is the reduced temperature. $k_{electronic}$ is assumed to be in the form given by [15]. k_{phonon} is formulated in terms of the semi-empirical models of A and B by [13, 14] as follows:

Coefficient $A(T_{irr}, T_{ann}, bu)$**.** [13] defines the coefficient A as:

$$A(T_{irr}, T_{ann}, bu) = \delta A + \Gamma(bu, GIS) + 0.046 \tag{2.2}$$

Note that [14] replaces 0.046 by 0.092623 for non-doped fuel ($gd = 0$) and $0.0524 + 0.3079 \times 10^{-2} gd + 12.2031 \times 10^{-4} gd^2$ for non-zero gadolinia additive where gd is the gadolinia content in wt.%.

The effect of the irradiation defects on A is defined in terms of the out-of-pile self-irradiation effect, δA_{Self} and the effective concentration of irradiation defects at end of life (EOL), δA_{EOL} as

$$\delta A = \delta A_{Self}(T_m, bu) + \delta A_{EOL}(T_m, bu) \tag{2.3}$$

where T_m is the maximum temperature of T_{irr} and T_{ann} (i.e., $T_m = \max(T_{irr}, T_{ann})$).

$$\delta A_{Self}(T_m, bu) = \begin{cases} 0.02F(bu) & \text{if } T_m \leq 900K \\ 0.02F(bu)\frac{1450 - T_m}{1450 - 900} & \text{if } 1450K > T_m > 900K \\ 0 & \text{if } T_m \geq 1450K. \end{cases} \tag{2.4}$$

$$\delta A_{EOL}(T_m, bu) = \frac{bu}{850}\left[\frac{1}{1 + \exp\left(\frac{T_m - 950}{25}\right)} + \frac{1}{1 + \exp\left(\frac{T_m - 1300}{35}\right)} - 0.0525\right] \tag{2.5}$$

$$F(bu) = \frac{1}{1 + \exp\left(\frac{20 - bu}{6}\right)} - 0.015267 \tag{2.6}$$

In [14], 0.015267 is replaced by 0.03444 in their formulation.

The contribution of non-volatile and volatile fission products is incorporated to the thermal conductivity model by [13, 14] as:

$$\Gamma(bu, GIS) = 9.02 \times 10^{-4} buGIS + 1.74 \times 10^{-3} bu + 7.51 \times 10^{-3} \tag{2.7}$$

where GIS is the fraction of volatile fission products present as dispersed atoms in the fuel matrix and is expressed by

$$GIS = \frac{1 - 0.9IRIM}{\left[1 + \exp\left(\frac{T_{irr} - 1350}{200}\right)\right]\left[1 + \exp\left(\frac{T_{ann} - 1350}{200}\right)\right]} \tag{2.8}$$

in terms of

$$IRIM = \frac{1}{\left[1 + \exp\left(\frac{T_{irr} - 950}{30}\right)\right]\left[1 + \exp\left(\frac{73 - bu}{2}\right)\right]}. \tag{2.9}$$

Coefficient $B(T_{irr}, T_{ann}, bu)$**.** [13] defines the coefficient B as:

$$B(T_{irr}, T_{ann}, bu) = B_0 + (B_1 - B_0)\left(1 - \frac{\delta B}{6.5 \times 10^{-5}}\right) \tag{2.10}$$

$$B_0 = -1.65 \times 10^{-6} bu + 2.55 \times 10^{-4} - 3.6 \times 10^{-5} IRIM \tag{2.11}$$

$$B_1 = 4.2 \times 10^{-7} bu + 2.75 \times 10^{-4} \tag{2.12}$$

In [14], 2.75×10^{-4} is replaced by 2.217×10^{-4} for non-doped fuel ($Gd = 0$) and for non-zero gadolinia additive, 2.75×10^{-4} is replaced by $2.553 \times 10^{-4} + 8.606 \times 10^{-6} gd - 0.0154 \times 10^{-4} gd^2$ where gd is the gadolinia content in wt.%.

$$\delta B = F(bu) \delta B_{EOL}(T_m, bu) \tag{2.13}$$

$$\delta B_{EOL}(T_m, bu) = \frac{bu}{34} \left[\frac{4.0 \times 10^{-5}}{1 + \exp\left(\frac{T_m - 950}{25}\right)} + \frac{2.5 \times 10^{-5}}{1 + \exp\left(\frac{T_m - 1300}{35}\right)} \right] \tag{2.14}$$

The correction is applied for the as-fabricated pores on thermal conductivity as [16, 17]:

$$k_0 = k_p \frac{1}{(1 - [2.6 - 5 \times 10^{-4} T_C]\, p)} \tag{2.15}$$

where T_C is the temperature (°C). The correction method for the conducting pores in the rim layer due to the HBS formation is discussed in Section 2.3.

To ensure that the model is implemented in BISON correctly and outputs reasonable values, we create thermal conductivity plots. Fig. 2.1 shows comparisons between the Ronchi, Staicu, and Staicu with 10 wt.% Gd at various temperatures. The models differentiate from each other slightly for the non-doped uranium dioxide fuel. The thermal conductivity increases in the transition region where the HBS starts to form. Staicu [18] attributes the increase in the thermal conductivity to the decrease in the fission gas concentration dissolved in the matrix. The degradation of the thermal conductivity resumes as a result of the accumulation of fission products for further increases in burnup.

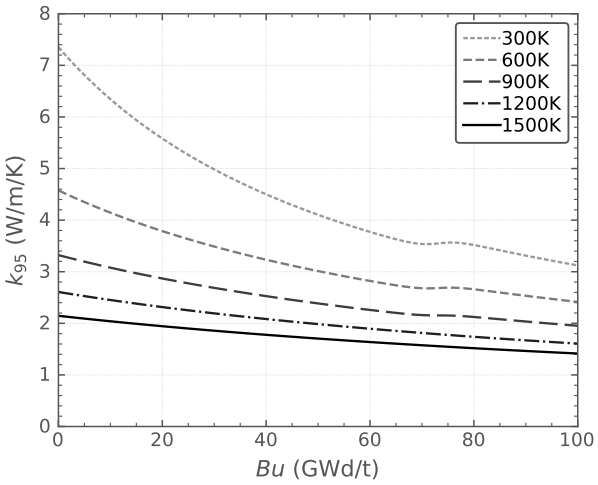

(a) The Ronchi model ($gd = 0$).

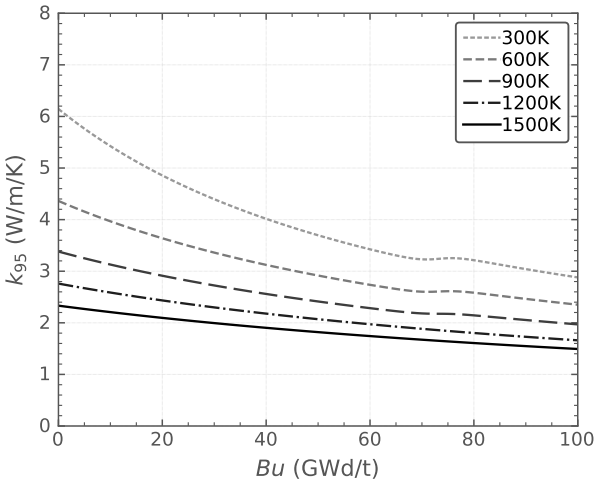

(b) The Staicu model ($gd = 0$).

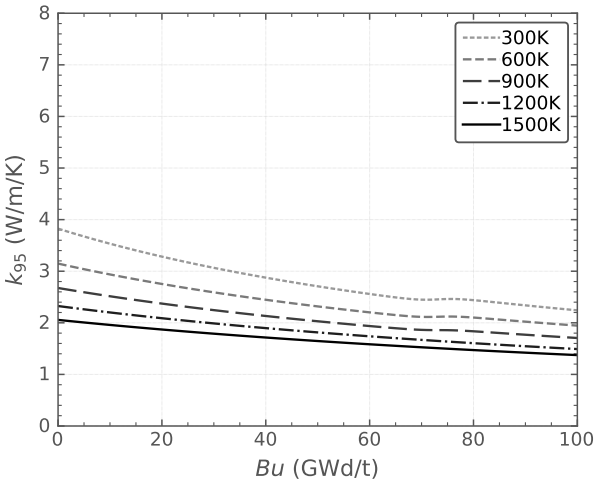

(c) The Staicu model ($gd = 10\,\mathrm{wt}\,\%$).

Figure 2.1: Comparison of the thermal conductivity model at $T = T_{irr}$ using (a) the Ronchi model, (b) the Staicu model, and (c) the Staicu model with an arbitrary gadolinia concentration of 10 wt.%.

2.2 High Burnup Structure Formation Model

In nuclear fuel under irradiation, in regions where substantial irradiation damage (high local burnup) is accompanied by a relatively low temperature, a dramatic change occurs to the as-fabricated microstructure. The restructuring involves the appearance of sub-micrometric grains free of extended defects and depleted of fission gas, and of micrometric gaseous pores at the grain boundaries. This phenomenon is referred to as *HBS formation* or, historically, *rim effect* [19, 20, 21]. The latter definition relates to the fact that the restructuring in light water reactor (LWR) UO_2 fuel starts at (and was originally thought to be limited to) the periphery of the pellet, where higher power density and burnup develop as a consequence of the fissile (^{239}Pu) concentration increase due to the capture of epithermal neutrons in the resonances of ^{238}U.

The formation of the HBS is gradual and depends on the local burnup and temperature. In particular, the HBS starts forming as a new phase within the regular fuel structure, with the local volume fraction of HBS progressively increasing with increasing local burnup. For example, Gerczak et al. [22] investigated the HBS formation in a PWR fuel rod irradiated to an average burnup of 72 MWd/kg_U through advanced electron microscopy techniques. In particular, they focused on the correlation between progressive grain polygonization[1] and grain boundary surfaces orientations. They showed that low-angle grain boundaries (LAGB) gradually transform into high-angle grain boundaries (HIGB) moving toward the pellet periphery (i.e., where HBS development is complete). The spatial distribution of grain boundary misorientations at various radial locations in the fuel pellet is shown in Fig. 2.2. Gerczak et al. [22] pointed out that the HBS is predominantly defined by HIGB, and the presence of LAGB indicates an incomplete transition to the HBS. The presence of local "in transition" areas is especially evident in the analysis at $r/r_o \sim 0.94$, while also noticeable in the mid-radial region to some degree (see Fig. 2.2) [22].

A new model has been implemented in BISON to describe the progressive formation of the HBS with increasing local burnup, also accounting for the temperature dependence of the restructuring process. In particular, the model computes the evolution of the local volume fraction of restructured (HBS) fuel, based on the approach proposed in [23]. The main features and equations of the model are described in Section 2.2.1 and an account of model testing is given in Section 2.2.2.

This new HBS model in BISON establishes a basis for the addition of any models describing phenomena that depend on HBS formation, including grain size, thermal conductivity, elastic modulus, gaseous porosity and swelling, and fragmentation/pulverization during accident situations such as the postulated LOCAs.

2.2.1 Model Description

The newly implemented BISON model `HighBurnupStructureFormation` computes the evolving HBS volume fraction in UO_2 (i.e, the ratio of the volume of restructured fuel to the total volume of fuel) as a function of burnup and temperature. This quantity is calculated locally at each BISON engineering mesh point,

[1] Polygonization is the subdivision of grains due to the arrangement of dislocations at the new restructured boundaries. Polygonization is thought to be responsible for the restructuring associated with HBS formation (e.g., [22]), although the re-crystallization mechanism has also been proposed.

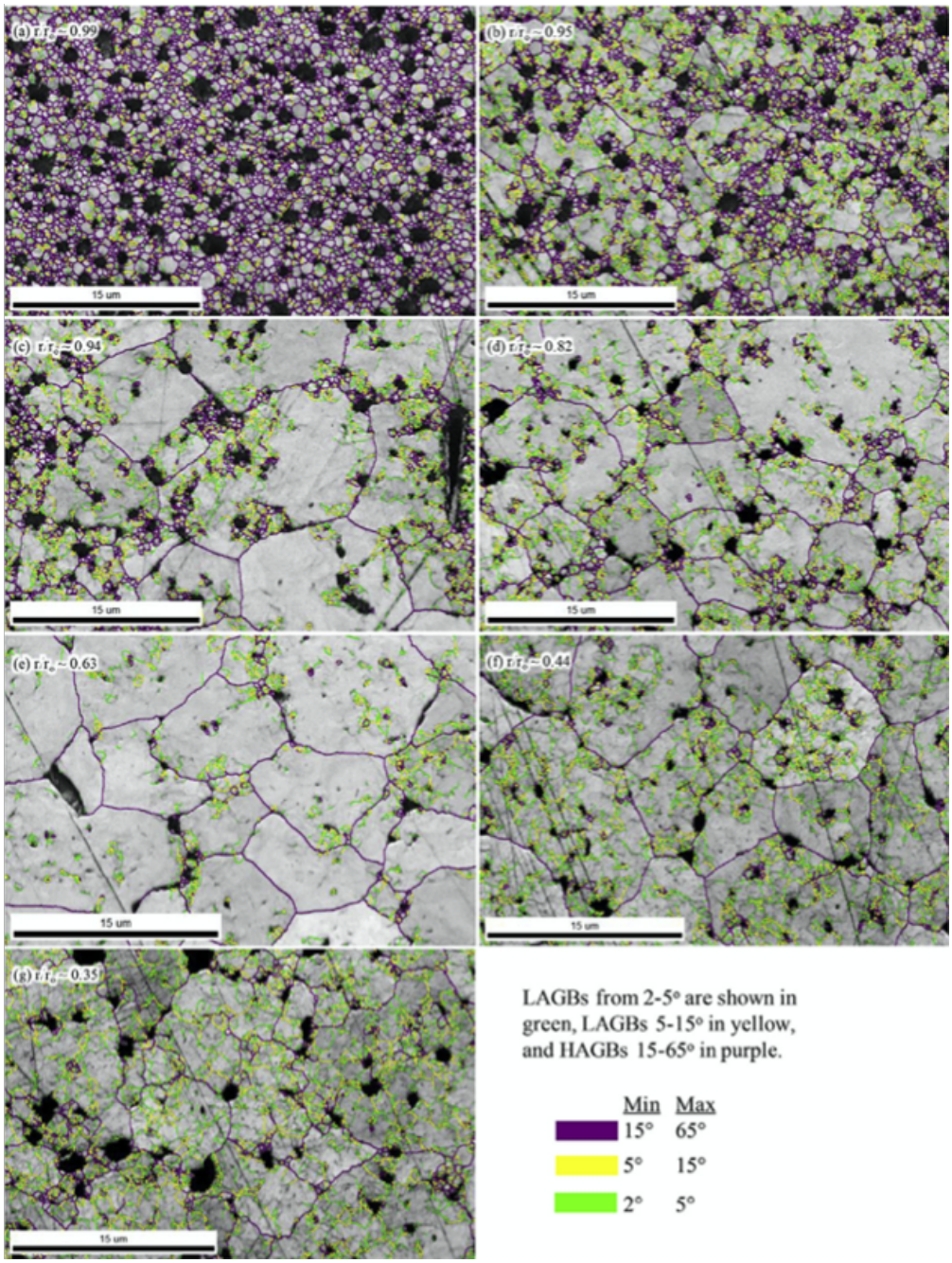

Figure 2.2: Grain boundary misorientation map overlaid on image-quality map for a UO_2 fuel pellet at relative radial positions r/r_0 from 0.99 to 0.35, (a) through (g). The analyzed fuel rod was irradiated in a PWR to 72 MWd/kg_U average burnup. High-angle grain boundaries are associated with the HBS. Taken from [22].

which represents a region of fuel large enough to contain a statistically significant number of microstructural features.

The new BISON capability, `HighBurnupStructureFormation` is based on the HBS formation model described in [23]. In particular, the volume fraction of HBS is computed as a function of the effective burnup (i.e., the burnup accumulated below a threshold temperature for thermal annealing of defects) which is calculated as:

$$bu_{eff} = \int H\left(T - T_{th}\right) dbu \tag{2.16}$$

where H is the Heaviside step function, T is the absolute temperature, T_{th} is the threshold temperature (e.g., the considered threshold temperature is 1273.15 K), and bu is the burnup.

The volume fraction of HBS is calculated using the Kolmogorov-Johnson-Mehl-Avrami (KJMA) formalism for phase transformations. The original KJMA formulation [24] is given by

$$\alpha = 1 - \exp\left(-Kt^{\gamma}\right) \tag{2.17}$$

where α is the volume fraction of the new phase, K is the transformation rate constant, t is the time, and γ is the so-called Avrami constant.

The specific expression proposed in [23] to describe HBS formation considers the effective burnup in place of the time and values for the constants based on fitting to experimental data for the restructured volume fraction derived from [22, 25]. The expression implemented in BISON is:

$$\alpha_{HBS} = 1 - \exp\left(-1.52 \times 10^{-7} bu_{eff}^{3.54}\right) \tag{2.18}$$

where α_{HBS} (-) is the volume fraction of HBS and bu_{eff} (MWd/kg$_{\mathrm{U}}$) the effective burnup (Eq. 2.16). Note that Eq. 2.18 corresponds to the model proposed in [23] with modified coefficients based on a later development.

The volume fraction of HBS as a function of the effective burnup according to Eq. 2.18 and the available experimental data are illustrated in Fig. 2.3.

2.2.2 Model Testing

Multiple test cases for the new HBS formation model in BISON have been completed. These test cases consist of idealized fuel irradiation simulations conceived to test and demonstrate the behavior of the model. This testing represents a necessary step preceding application of the model to BISON simulations of experimental fuel rod irradiation cases for code validation (Chapter 4). Descriptions for the test cases, results, and discussion are presented below.

2.2.2.1 Local Behavior Simulations

Two test cases have been considered to test the model through the simulation of local behavior under idealized fuel irradiation conditions:

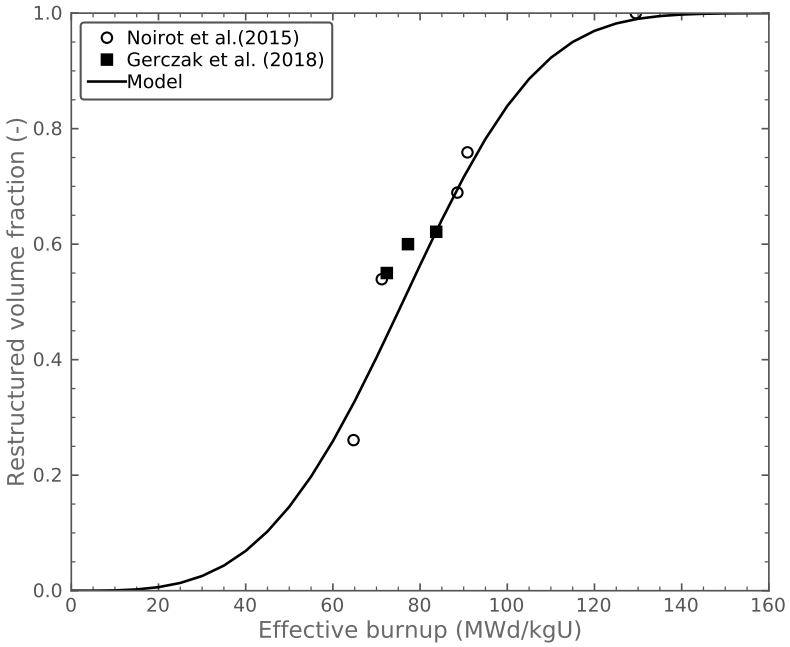

Figure 2.3: Volume fraction of HBS as a function of the effective burnup according to the model implemented in BISON and based on [23]. Experimental data derived from [22, 25] in [23] and used for model fitting are also shown.

- **Test 1:** Irradiation at constant temperature below the threshold temperature for effective burnup accumulation (Section 2.2.1). In particular, the temperature is kept constant at 1173 K. The applied fission rate is constant at 2×10^{19} $\mathrm{m}^{-3}\mathrm{s}^{-1}$. The considered total irradiation time is 2×10^8 s ≈ 6.3 years. The expected results are: (i) a linearly increasing effective burnup that coincides with the burnup (Eq. 2.16); and correspondingly, (ii) a monotonically increasing HBS fraction according to Eq. 2.18.
- **Test 2:** Irradiation at varying temperature with periods below and above the threshold temperature. In particular, the temperature is kept below the threshold temperature of 1273.15 K for time $t < 1.00 \times 10^8$ s and $t > 1.75 \times 10^8$ s, and above the threshold temperature for 1.00×10^8 s $< t < 1.75 \times 10^8$ s. The two transients consist of linear variations at a constant rate of 2×10^{-5} K/s between the reference low and high temperatures of 1173.15 K and 1373.15 K, respectively. As with Test 1, the fission rate is kept constant at 2×10^{19} $\mathrm{m}^{-3}\mathrm{s}^{-1}$ and the considered total irradiation time is 2×10^8 s ≈ 6.3 years. The expected results are: (i) an effective burnup that increases only during the periods with the temperature below the threshold and remains constant otherwise (Eq. 2.16); and (ii) an HBS fraction that increases with increasing effective burnup according to Eq. 2.18.

Fig. 2.4 shows the temperature history and calculated effective burnup for these two test cases. Note that the computational domain is a unity finite element for both cases. For Test 1, the calculated effective burnup coincides with the burnup and increases linearly with time, reaching a value of 0.1721 FIMA, or

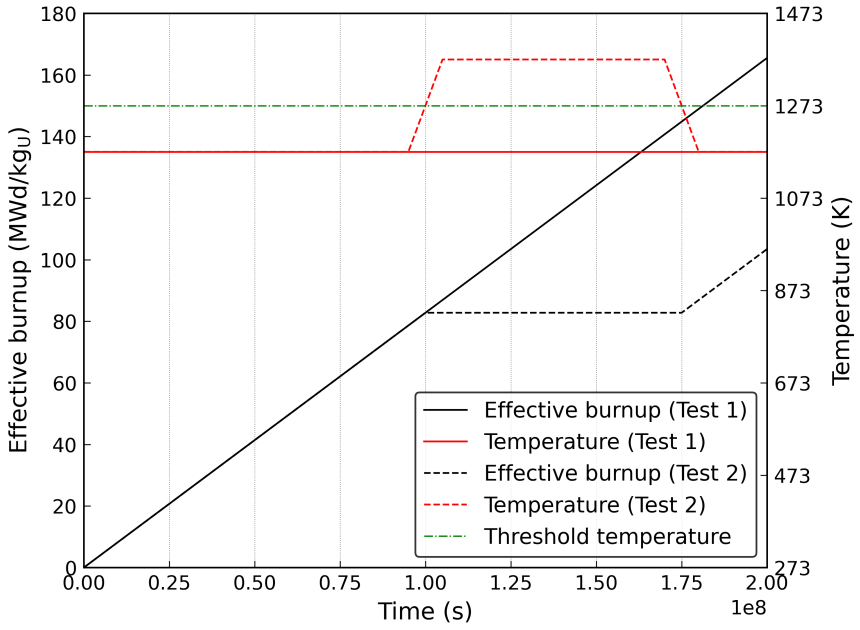

Figure 2.4: Temperature history and calculated effective burnup for two BISON test cases for the HBS formation model.

165.5 MWd/kgU, at the end of the simulation at 2×10^8 s. For Test 2, the calculated effective burnup is the same as with Test 1 during the first half of the irradiation (i.e., until the temperature crosses the threshold temperature of 1273.15 K at 1.00×10^8 s). During the period with the temperature above the threshold temperature, the effective burnup remains constant. Once the temperature decreases back below 1273.15 K at 1.75×10^8 s, the effective burnup starts increasing again. The effective burnup reaches a value of 0.1076 FIMA, or 103.5 MWd/kgU, at the end of the simulation. During the periods with temperature below the threshold, the increased rates of the burnup and effective burnup coincide. These results confirm the expected model behavior, in accordance with Eq. 2.16.

Fig. 2.5 shows the temperature history and calculated volume fraction of HBS for the two test cases. For Test 1, the calculated fraction of HBS increases monotonically with the linearly increasing effective burnup as the temperature remains below the threshold. In particular, the HBS fraction takes values of 0.077, 0.608, 0.980 and 1.000 after 0.5×10^{-5}, 1.0×10^{-5} s, 1.5×10^{-5} s and 2.0×10^{-5} s, respectively. For Test 2, the calculated fraction of HBS increases only during the periods with the temperature below the threshold (i.e., with increasing effective burnup). The HBS fraction takes values of 0.077, 0.608 and 0.873 after 0.5×10^{-5} s, 1.0×10^{-5} s and 2.0×10^{-5} s, respectively. These results also confirm that the model correctly produces the expected behavior, in accordance with Eq. 2.18.

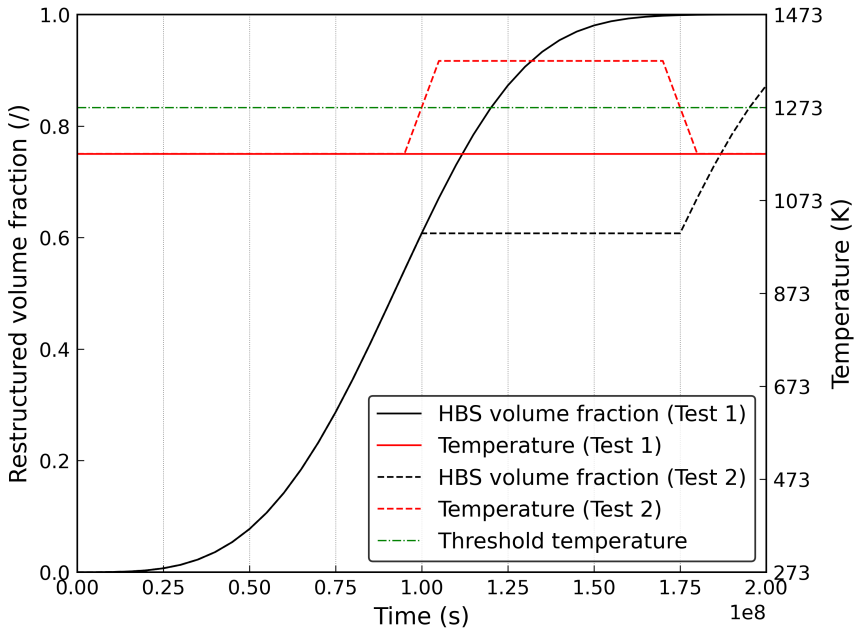

Figure 2.5: Temperature history and calculated volume fraction of HBS for two BISON test cases for the HBS formation model.

2.2.2.2 Single-Pellet Irradiation Case

As a more complex example case for the application of the HBS formation model relative to the single-element (local) calculations presented in Section 2.2.2.1, irradiation of a single LWR fuel pellet was simulated with BISON. Relative to the local calculations in Section 2.2.2.1, the single-pellet case is intended to demonstrate the behavior of the model within a more complete BISON simulation that also includes radial power and burnup profile calculations, as well as thermal and mechanical fuel analyses. The burnup profile calculation, in particular, is directly coupled to the HBS formation model as the latter depends on the calculated local burnup (Section 2.2.1). The simulation is expected to represent the burnup peaking effect at the pellet periphery through the existing BISON burnup model and, in turn, the development of the HBS at the pellet rim through the new model. The temperature dependence of the HBS formation model is also exercised. In particular, the radial temperature profile is calculated through the BISON thermal analysis, with only the lower-temperature, peripheral region of the pellet expected to accumulate significant effective burnup and HBS volume fraction due to the temperature threshold in the new HBS model (Section 2.2.1). This single-pellet irradiation case is thus aimed at reproducing the fundamental physical coupling between burnup peaking at the pellet rim, temperature distribution, and HBS formation, through the new HBS model applied within a realistic fuel thermo-mechanics and burnup behavior simulation with BISON.

The developed test case consists of a UO_2 pellet of 10 mm height and 4.1 mm radius, represented in 2D with 10 axial elements and 40 radial elements. The mesh is refined radially toward the pellet periphery, to

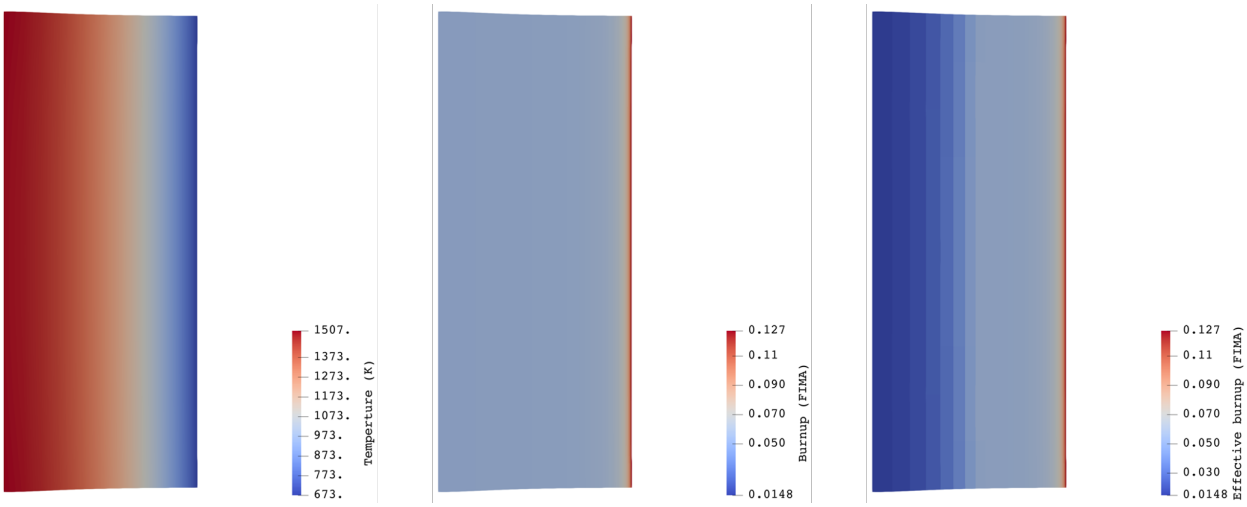

Figure 2.6: Results of the single-pellet irradiation case at the final time of the simulation (3 years) for temperature (left), burnup (center), and effective burnup (right).

more accurately capture the burnup peaking and associated HBS formation profile. The applied linear heat rate increases from zero to 25 kW/m during the first 3 hours and is then kept constant until the completion of a 3-year simulated irradiation. The pressure at the outer (radial) pellet surface is increased from 1.0 to 2.5 MPa during the initial rise to power, then kept constant, to simulate the fill-gas pressure in a simplified manner. The temperature at the outer (radial) surface of the pellet is kept constant at a value of 673 K, realistic for LWR fuel. The BISON thermo-mechanical analysis includes temperature and burnup-dependent thermal conductivity, thermal expansion, relocation, densification, swelling, and creep strains [26]. The burnup distribution is calculated using the `BurnupFunction` model in BISON [26]. As mentioned previously, the `HighBurnupStructureFormation` model computes the effective burnup and volume fraction of HBS as a function of the local burnup and temperature.

Fig. 2.6 shows contour plots of results for temperature, burnup, and effective burnup at the final time of the simulation (3 years). The temperature at the pellet center is $\approx$ 1507 K, which is higher than the threshold temperature of 1273.15 K for effective burnup accumulation. The burnup is maximum at the pellet periphery, where it reaches a value of 0.127 FIMA $\approx$ 122 MWd/kg$_{\mathrm{U}}$. The calculated pellet average burnup is 0.059 FIMA $\approx$ 56 MWd/kg$_U$. The effective burnup is also maximum at the pellet periphery and equal to the maximum burnup of 0.127 FIMA $\approx$ 122 MWd/kg$_{\mathrm{U}}$. This is consistent with the effective burnup equation (Eq. 2.16), considering that the temperature in the peripheral region of the pellet remains below the threshold temperature throughout the simulation. As seen in Fig. 2.6 (right), the effective burnup differs from (is lower than) the burnup in the central region of the pellet. Here, the temperature exceeds the threshold during at least part of the simulation, and the effective burnup is not incremented during the periods with the local temperature above the threshold (Eq. 2.16).

Fig. 2.7 shows the contour plot of results for the volume fraction of HBS at the final time of the simulation

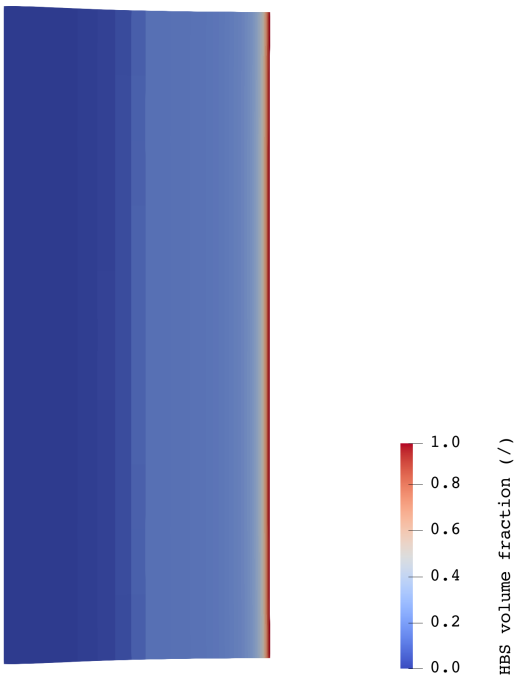

Figure 2.7: Results of the single-pellet irradiation case at the final time of the simulation (3 years) for the volume fraction of restructured fuel (HBS).

(3 years). As the effective burnup is maximum at the pellet periphery (Fig. 2.6) and the HBS volume fraction increases with increasing effective burnup, the HBS volume fraction is maximum at the pellet periphery. More precisely, a maximum HBS volume fraction of ≈ 0.98 is calculated at the outer edge of the pellet. The results of this simulation demonstrate a qualitatively correct representation of the actual fuel behavior in-reactor, with the HBS developing from the pellet rim due to the burnup peaking effect.

2.3 Ad-hoc Porosity Formation Model

Our current approach uses an ad-hoc porosity model to capture the porosity evolution due to the HBS formation. We calibrate a surrogate model that is obtained from measured local burnup and measured porosity. The computational model for the porosity is chosen as:

$$p(Bu) = \theta_1 \ln(Bu) + \theta_2 + \epsilon \tag{2.19}$$

where Bu is the local burnup (GWd/t), $\boldsymbol{\theta} = \{\theta_1, \theta_2\}$ is the coefficient matrix to be determined, and the observed error is normally distributed around zero as $\epsilon \sim \mathcal{N}\left(0, \boldsymbol{I}\sigma^2\right)$.

The motivation in statistical inference is to draw conclusions about a phenomenon based on observed data, $\boldsymbol{v} = \{v\}_{i=1}^n$. The interpretation of probability is subjective and updated with the new data set. In the parameters estimation, the parameters, $\boldsymbol{\theta} = \{\theta\}_{i=1}^n$ are described as densities. Model parameters and their correlations with each other are explored by employing optimization algorithms: frequentist and Bayesian methods. The frequentist results are used as a prior to the delayed rejection adaptive Metropolis (DRAM) calibration—a Bayesian approach—and the results from DRAM are used in this study as the final model coefficient estimates for the surrogate model of interest (i.e., Eq. 2.19 for this study).

The calibration is performed with the available experimental data in the literature. The estimates are constructed using 1×10^4 DRAM iterations with a burn-in period of 1×10^4 iterations. The initial coefficient matrix is chosen to be $\boldsymbol{\theta}_{initial} = \{1.1270 \times 10^{-1}, -4.1710 \times 10^{-1}\}$ with a resulting variance of $\sigma^2 = 0.015527$. The marginal densities are plotted along with the initial guesses. Marginal parameter distributions for the porosity are given in which all parameters are summarized by their mean (μ), their standard deviation (σ), and the variance (σ^2) of the observed error. Fig. 2.8 shows the Markov Chain Monte Carlo (MCMC) chains and marginal densities obtained from both frequentist and DRAM approaches.

The DRAM calibration results are summarized in terms of $\mu \pm 1\sigma$ as:

$$\boldsymbol{\theta}_{DRAM} = \{1.1452 \times 10^{-1} \pm 7.1638 \times 10^{-3}, -4.2520 \times 10^{-1} \pm 3.2924 \times 10^{-2}\} \tag{2.20}$$

with a resulting variance, σ^2 of 0.015799.

The model comparison to the experimental data is shown in Fig. 2.9. The porosity, p is given by Eq. 2.19 with the estimated model coefficients given in Eq. 2.20.

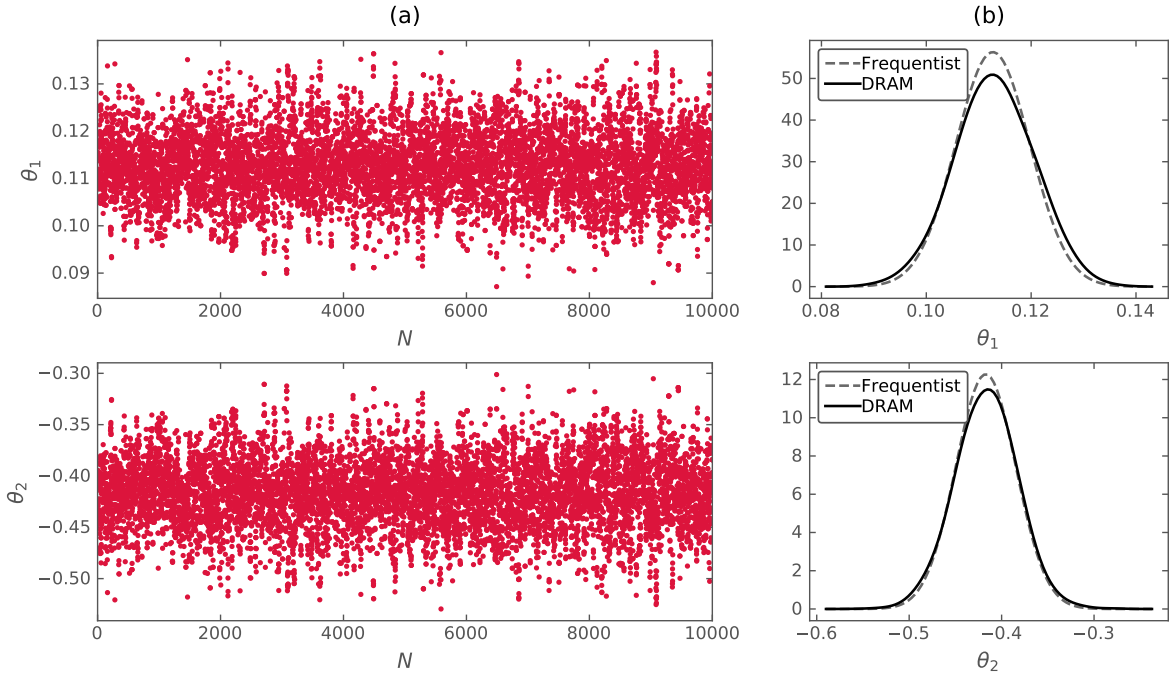

Figure 2.8: (a) MCMC chains and (b) marginal densities for the coefficient matrix $\boldsymbol{\theta} = \{\theta_1, \theta_2\}$ of Eq. 2.19.

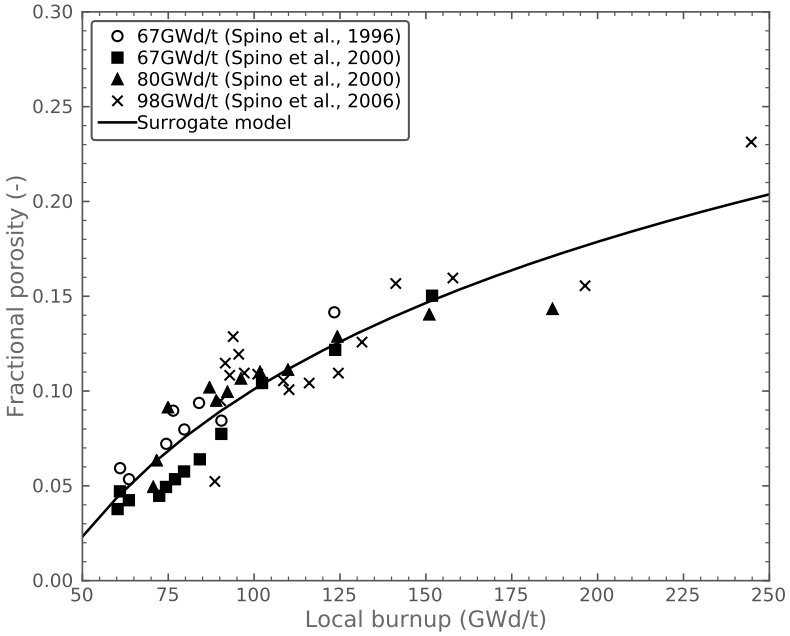

Figure 2.9: A comparison of the surrogate model as a function of local burnup (*experimental data from [27, 28, 29]*).

2.4 Correction Methods for the Conducting Pores

The rim thermal conductivity is computed using two methods according to

1. The first method by Kämpf [30], referred to as `KAMPF` model in BISON:

$$k_{rim} = k_0 \left(1 - p^{2/3} \left[1 - \frac{1}{1 + p^{1/3} \left(\frac{k_0}{k_p} - 1 \right)} \right] \right) \tag{2.21}$$

2. The second method by Lee et al. [31, 32, 33], referred to as `LEE` model in BISON:

$$k_{rim} - (1 - p) \left(\frac{k_0 - k_p}{k_0^{1/3}} \right) k_{rim}^{1/3} - k_p = 0 \tag{2.22}$$

where k_{rim} is the rim thermal conductivity, k_p is the thermal conductivity of conducting pores, p is the porosity (-), and k_0 is the thermal conductivity of the material. It is assumed that the pores are filled with the monatomic inert gas, xenon. Thus, the pore thermal conductivity is computed using the following relation [34]: $k_p(T) = 4.351 \times 10^{-5} T^{0.8616}$ in terms of the temperature, T (K).

Note that the second method is expressed in terms of a third-order polynomial. The rim thermal conductivity is computed by solving this cubic equation given in Eq. 2.22. For this cubic equation, there may be three possible solutions: (i) single real root, (ii) three real roots, or (iii) one real and two complex roots. The highest real root is assigned for the rim thermal conductivity, k_{rim}. We employ a root-finding algorithm to solve the cubic equation analytically. The analytical solution can be found in the literature [35]. Roots of the third-order polynomial are computed in the code in the following order (Algorithm 1), given by [36].

Algorithm 1 Algorithm to find the largest real root of the cubic equation to assign the gas density analytically [36].

procedure
  initialize $\boldsymbol{Re} = \{0.0\}$ and $\boldsymbol{Im} = \{0.0\}$,
  compute $p = \frac{(b^2 - 3ac)}{9a^2}$; $q = \frac{(9abc - 27a^2d - 2b^3)}{54a^3}$; offset $= \frac{b}{3a}$,
  compute the discriminant, $\Delta = (p^3 - q^2)$,
  if $\Delta > 0$ **then**
    compute $\theta = \arccos\left(\frac{q}{p\sqrt{p}}\right)$; $r = 2\sqrt{p}$
    for $n = 1, 2, 3$ **do**
      compute $Re[n] = r \cos\left(\frac{\theta + 2[n-1]\pi}{3.0}\right) -$ offset; $Im[n] = 0.0$
  else
    compute $\gamma_{1,2} = (q \pm \sqrt{-\Delta})^{1/3}$
    compute $Re[1] = (\gamma_1 + \gamma_2) -$ offset; $Re[2] = Re[3] = -\frac{1}{2}(\gamma_1 + \gamma_2) -$ offset
    if $\Delta \neq 0$ **then**
      calculate the complex conjugate roots $Im[2] = \frac{\sqrt{3}}{2}(\gamma_1 + \gamma_2)$ and $Im[3] = -\frac{\sqrt{3}}{2}(\gamma_1 + \gamma_2)$
  return the maximum real value, $\max(\boldsymbol{Re})$

To compare the aforementioned methods for the porosity corrections on the thermal conductivity, given

measured porosity profiles from [27, 29] at a variety of average fuel burnups. Fig. 2.10 shows the experimental data and corresponding reduction on the thermal conductivity using both methods. Method 2 results in a conservative reduction of the thermal conductivity as compared to the Method 1.

Validity of Algorithm 1. The cubic equation with real coefficients is given by $ax^3 + bx^2 + cx + d = 0$ with $a \neq 0$. The hard-coded numerical solution in C++ for the root-finding (given in Algorithm 1) is compared against the results from the libraries in Python and the expected results. The procedure in Python [37] is relatively easier with the use of `numpy` libraries [38]. The cubic equation is introduced as `roots= np.roots([a, b, c, d])` in the code. The largest real root is computed as `maxRealRoot= np.max(roots[np.isreal(roots)]).real`. Some examples are provided in Table 2.1. The results are in good agreement with the expected results. Note that this exercise was previously performed by [36] for the calculation of gas density using the virial expansion form of the ideal gas law in terms of the macroscopic thermodynamic properties and particle interactions [39].

Table 2.1: Comparison of the largest real value that is indicated by the bold numerical value [36]. The cubic equation is given by $ax^3 + bx^2 + cx + d = 0$.

$\{a, b, c, d\}$	Hard-coded Algorithm 1 in C++	Python	Cubic Equation Solver [40]
$\{1, 3, 3, 1\}$	**-1.00000**	-1.00000+5.68937e-6·j -1.00000-5.68937e-6·j **-1.00001**	**-1.0000**
$\{1, -3, 3, -1\}$	**1.00000**	1.00000+5.69146e-6·j 1.00000-5.69146e-6·j **1.00001**	**1.0000**
$\{2, 3, -8, 3\}$	-3.00000 0.50000 **1.00000**	-3.00000 0.50000 **1.00000**	-3.0000 0.5000 **1.0000**
$\{1, 5, 5, -28\}$	-3.35223+2.27817·j -3.35223-2.27817·j **1.70446**	-3.35223+2.27817·j -3.35223-2.27817·j **1.70446**	-3.3522+2.2782·j -3.3522-2.2782·j **1.7045**

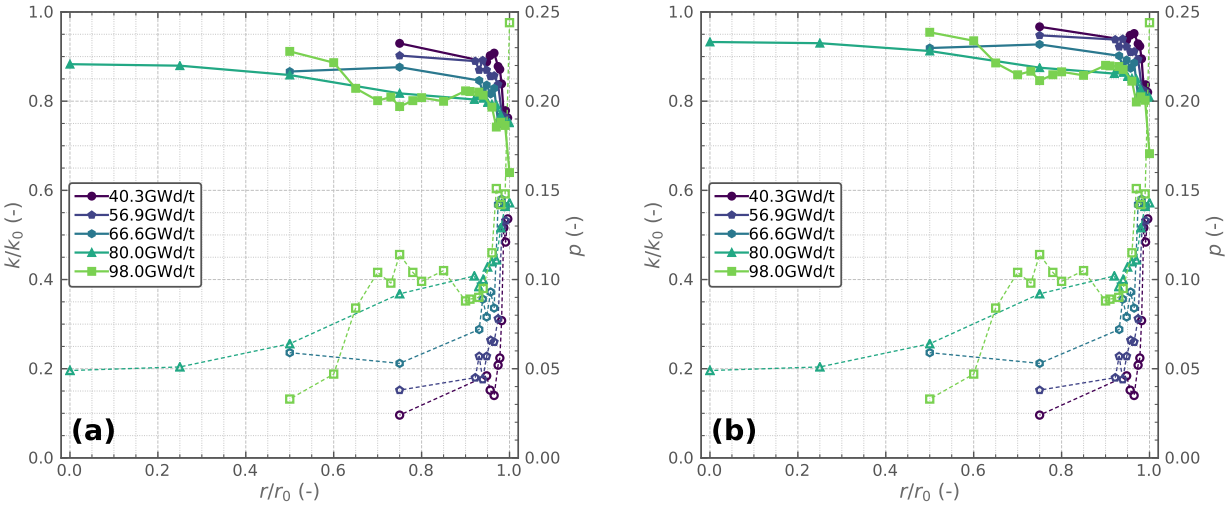

Figure 2.10: Comparison of thermal conductivity reductions (*solid lines*) using (a) the first method and (b) the second method for the porosity correction given measured radial porosity profiles (*dashed lines*) at varied average fuel burnups [27, 29]. The thermal conductivity of the xenon-filed pores is assumed to be 0.25 W/m/K. The numerical values are tabulated below.

Ref.	Average burnup (GWd/t)	Radial position r/r_0 (-)	Measured porosity p (-)	**Method I** Computed k/k_0 (-)	**Method II** Computed k/k_0 (-)
[27]	40.3	0.996	0.134	0.763	0.820
		0.991	0.121	0.779	0.837
		0.987	0.129	0.769	0.827
		0.982	0.077	0.839	0.895
		0.978	0.056	0.871	0.923
		0.974	0.052	0.878	0.929
		0.965	0.035	0.908	0.952
		0.956	0.038	0.902	0.948
		0.948	0.046	0.888	0.937
		0.750	0.024	0.930	0.967
[27]	56.9	0.991	0.133	0.764	0.821
		0.983	0.129	0.769	0.827
		0.974	0.078	0.837	0.894
		0.965	0.065	0.857	0.911
		0.957	0.066	0.856	0.910
		0.948	0.057	0.870	0.922
		0.939	0.044	0.892	0.940
		0.931	0.057	0.870	0.922
		0.922	0.045	0.890	0.938
		0.750	0.038	0.902	0.948
[27]	66.6	0.991	0.141	0.754	0.811
		0.982	0.145	0.749	0.806
		0.974	0.142	0.753	0.810
		0.965	0.084	0.829	0.886
		0.957	0.093	0.816	0.874
		0.948	0.079	0.836	0.892
		0.939	0.089	0.822	0.879
		0.931	0.072	0.846	0.902
		0.750	0.053	0.876	0.927
		0.500	0.059	0.866	0.919
[29]	80.0	1.000	0.143	0.752	0.808
		0.990	0.141	0.754	0.811
		0.980	0.129	0.769	0.827
		0.970	0.111	0.792	0.850
		0.960	0.110	0.793	0.851
		0.950	0.107	0.797	0.855
		0.940	0.100	0.806	0.864
		0.930	0.096	0.812	0.870
		0.920	0.102	0.804	0.862
		0.750	0.092	0.817	0.875
		0.500	0.064	0.859	0.912
		0.250	0.051	0.880	0.930
		0.000	0.049	0.883	0.933
[29]	98.0	1.000	0.244	0.640	0.682
		0.990	0.148	0.746	0.802
		0.980	0.142	0.753	0.810
		0.970	0.151	0.742	0.798
		0.960	0.115	0.787	0.845
		0.940	0.095	0.813	0.871
		0.930	0.090	0.820	0.878
		0.910	0.089	0.822	0.879
		0.900	0.088	0.823	0.880
		0.850	0.105	0.800	0.858
		0.800	0.099	0.808	0.866
		0.780	0.104	0.801	0.859
		0.750	0.114	0.788	0.846
		0.730	0.098	0.809	0.867
		0.700	0.104	0.801	0.859
		0.650	0.084	0.829	0.886
		0.600	0.047	0.886	0.935
		0.500	0.033	0.912	0.955

3. Verification

Verification is a process to ensure that the code functions correctly and is reliable. BISON has undergone rigorous verification and validation activities [41, 42, 43, 44]. Here we provide a verification problem to assess finite-element solutions of BISON, and correspondingly, MOOSE. Detailed information on the verification methodology can be found in [44] including an extensive set of verification problems, which is briefly outlined in Section 3.1. The selected verification problem is provided in Section 3.2. The problem is set up and solved in BISON to test the underlying mathematical model. This is achieved through a quantified demonstration that code results converge to a reference solution at the theoretical rate as the computational mesh is refined. The results and discussion are provided in Section 3.3.

3.1 Procedure

The first task in the verification procedure is the selection of a reference solution. In this work, we employ the *method of exact solutions (MES)* [45], which requires a known solution. It's difficult to find an analytic solution to a complex nonlinear differential equation. Therefore, significant simplifying assumptions are necessary to obtain the solution of these equations. The verification problem that we choose in this work is provided in Section 3.2, which focuses on the heat conduction solution in BISON.

The theoretical rate of convergence (or the formal order of accuracy) can be determined through analysis of the linear truncation error (LTE). After we select the method to obtain a reference solution, the theoretical convergence rate of the numerical algorithm is established. More discussion can be found in [44] on how to derive the formal order of accuracy for the finite element method (FEM).

A numerical representation of the mathematical model is formulated and solved on at least three consecutive meshes. Then, we compute the differences between the numerical solutions and the reference solution using the global error norms. For instance, the L_2-norm (or Euclidean norm) of the error over the solution domain Ω is defined as

$$||q|| = \left[\int_{\Omega} (q - \tilde{q})^2 \mathrm{d}\Omega\right]^{1/2}, \tag{3.1}$$

where the reference solution is represented by the primary variable q (e.g., temperature for heat conduction, displacement for mechanics, etc.) and the numerical approximation is $\tilde{q}$.

The local LTE converges at some rate; therefore, the global error will converge at the similar rate. To

relate the error to the characteristic element size h, we use the relation of $||q|| = Ch^{\hat{p}}$ where C is an arbitrary problem-dependent constant and $\hat{p}$ is the observed order of accuracy. This relation is in a power law form; therefore, the slope of the error on a log-log plot is equivalent to the observed order of accuracy $\hat{p}$:

$$\hat{p} = \frac{\log\left(||q||_{rh}/||q||_h\right)}{\log\left(r\right)} \tag{3.2}$$

where $||q||_h$ is the norm of q at some mesh size h and r is the mesh refinement factor ($r \geq 2$).

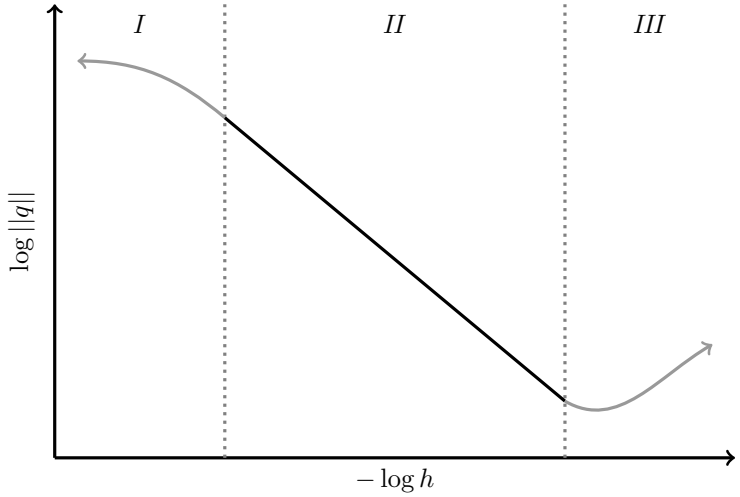

Figure 3.1: A pictorial representation of expected convergence behavior [44] that is characterized by three regions in practical applications [46]: *Region I* represents coarse meshes, *region II* is the asymptotic region, and *region III* is caused by numerical error. The desirable region for the numerical solutions is the asymptotic region.

3.2 Exact Solution to the Mathematical Problem

This verification problem is a modification of the problem given in [44, Problem 3.7] and [47, p.194]. The thermal conductivity of a solid body varies linearly with temperature: $k = k_0^\star(1 + \beta T)$, where $\beta > 0$, and k_0 is an arbitrary constant. Here, we assume $k_0^\star = k_0(1 - p)$ in terms of the fractional porosity p which is different than the original form with k_0. This alteration will not affect the final temperature distribution since the porosity multiplier is not a function of temperature. The solid body has a constant internal heat generation q''' and the same constant temperature is imposed on both surfaces: $T(r_i) = T(r_o) = T_o$ at the inside radius r_i and the outside radius r_o, respectively. In thermal equilibrium, the analytic solution for the temperature distribution becomes

$$T(r) = T_o + \frac{1}{\beta}\left\{\sqrt{1 + \frac{q'''\beta}{2k_0^\star}\left[(r_o^2 - r^2) - (r_o^2 - r_i^2)\frac{\ln\left(r_o/r\right)}{\ln\left(r_o/r_i\right)}\right]} - 1\right\}, \tag{3.3}$$

where $0 < r_i \leq r \leq r_o$.

The verification methods typically require significant simplifying assumptions to solve the differential equation. In this problem, the porosity multiplier is chosen as $(1 - p)$ to simplify the mathematical setup and obtain an analytical solution to the problem, which is representative of typical porosity correction methods [48, 30].

3.3 Results & Discussion

The problem is solved in BISON on the domain $\vec{X} \in [0.2, 1]$ using Dirichlet boundary conditions $T(0.2) = T(1) = T_o = 0\,\mathrm{K}$. Steady-state heat conduction is considered using a nonlinear thermal conductivity where $k_o = 1\,\mathrm{W/m/K}$ and the porosity fraction is assumed as $p = 0.05$. The mathematical problem is setup in a BISON input file. Then, the numerical simulations are obtained at many mesh densities using first-order and second-order, one-dimensional FEs: `EDGE2` and `EDGE3`, respectively.

In Fig. 3.2, the exact and computed solutions are shown for three different meshes and two finite element types (first order, or linear, with two nodes per element; second order, or quadratic, with three nodes per element).

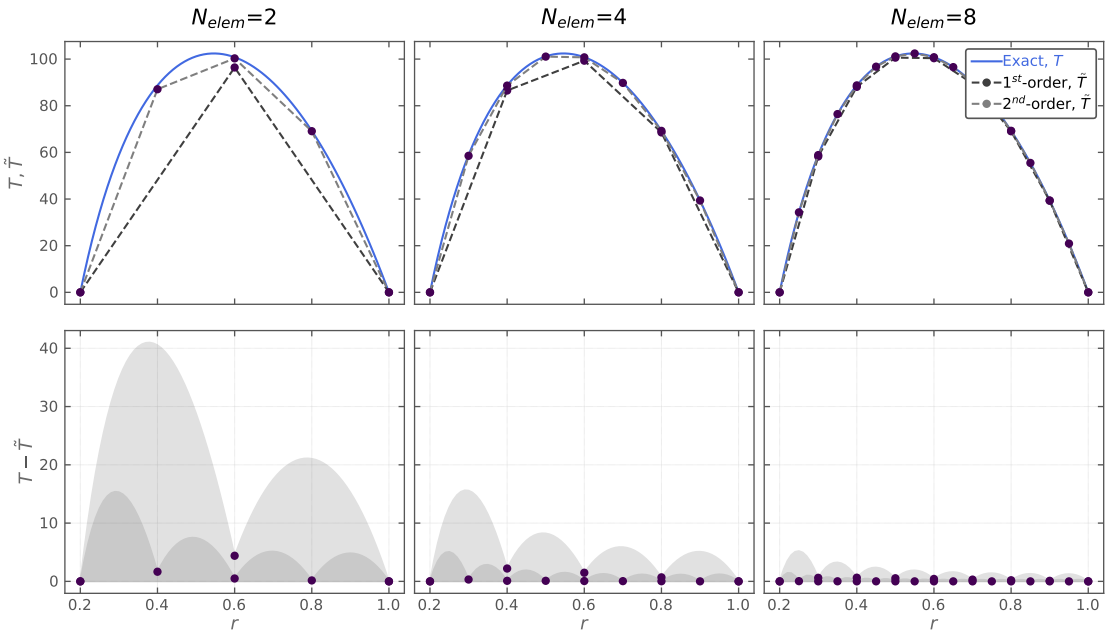

Figure 3.2: Temperature distributions (*first row*) and residual (*second row*) for different meshes and finite elements.

A convergence study is conducted with a refinement factor of two ($r_r = 2$). The computed norms for each FE type and boundary condition type are plotted in Fig. 3.3. Note that the L_2-norm quantifies convergence

of the temperature distribution (*solid lines*) and the H_1-norm quantifies convergence of the heat flux (*dashed lines*). Slopes of first-, second-, and third-order convergence are indicated. The formal order of accuracy is two for linear FEs and three for quadratic FEs for the temperature solution and one less for the heat flux solution. In the asymptotic region for both cases, the linear and quadratic FE solutions converge to the exact solution with the correct order of accuracy.

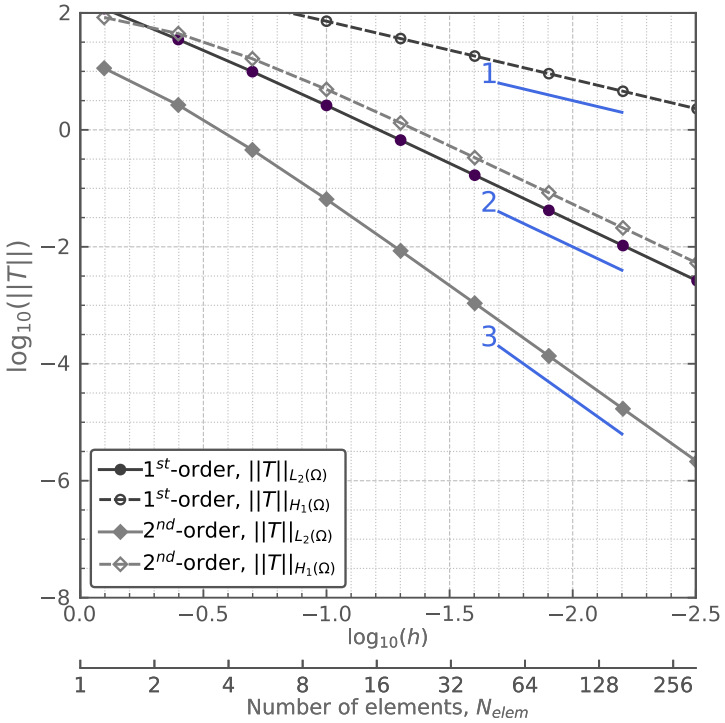

Figure 3.3: Convergence plot ($r_r = 2$)

4. Validation

Validation is the process of comparing model predictions to experimental measurements to determine the applicability of the model to real-world applications. Industry wants to push the average operational burnup limit from the current 62 MWd/kgU level to 68 MWd/kgU, and potentially 75 MWd/kgU. Therefore, integral rod experimental validation of fuel performance models is necessary. At present, limited integral rod data exist at these burnups, with the Studsvik [49, 50] and Halden [51] programs providing the majority of data available. In this chapter, we validate the newly added models in Chapter 2 to two rods selected from the IFA-650 LOCA test series conducted at the Halden reactor in Norway. The tests investigated here include IFA-650.4 and IFA-650.9.

4.1 Experimental Measurements

In total, 15 tests have been completed as part of the IFA-650 LOCA test series. Each test was designed for a specific purpose by varying operational conditions, pre-irradiation history, plenum size, and cladding type to explore the impact of these various phenomena on the behavior of the fuel rod during a LOCA. Prior to the writing of this report, tests IFA-650.2, IFA-650.9, and IFA-650.10 were analyzed using BISON. The selection of these tests was primarily driven by the BISON team's participation in the Fuel Modelling in Accident Conditions (FUMAC) project [52]. In this report a new case IFA-650.4 was selected for two reasons: (1) the pre-irradiation achieved a sufficient burnup to use as validation of the HBS formation and thermal conductivity models described in this report; and (2) the rod experienced severe axial relocation of the fragmented fuel providing additional validation for the axial relocation model added to BISON a few years ago [53]. The second case discussed in this report is a revisit of the IFA-650.9 test to evaluate the impacts on the results from the inclusion of the latest model developments in HBS formation and high-burnup thermal conductivity models introduced previously in this report.

The IFA-650.4 test was the fourth test completed as part of the LOCA test series. The purpose of the test was to repeat the conditions of the IFA-650.3 test on a pre-irradiated fuel rod to assess the validity of existing LOCA safety criteria [54]. In particular, the experiment was designed in such a way to maximize the balloon size to promote fuel relocation and assess the impacts on cladding temperature and oxidation. The average burnup of the fuel after the base irradiation was ~ 92 MWd/kgU.

Due to the high burnup of the pre-irradiated fuel, severe fragmentation and axial relocation were observed

during the transient. A large cladding balloon was also observed through gamma scans after the conclusion of the experiment. The maximum measured internal pressure was ~ 7.1 MPa achieved around 265–270 seconds after blowdown occurred. Cladding rupture occurred at ~ 366 s after blowdown.

The IFA-650.9 test was the ninth test completed as part of the LOCA test series. The purpose of this test was similar to IFA-650.4 and was actually used to clarify and confirm the behavior of significant fuel relocation that was observed in the previous test. The burnup of the fuel after the base irradiation was $\sim$ 89.9 MWd/kgU. Cladding ballooning was observed to begin at $\sim$106 s after blowdown at a maximum pressure of ~ 7.33 MPa and failure of the cladding occurred at $\sim$133 s after blowdown at a cladding temperature of ~ 1083 K.

The fabrication characteristics of the IFA-650.4 and IFA-650.9 specimens are provided in Table 4.1. Segmented from PWR mother rods in both cases, the cladding material consisted of a Zry-4 base with a 100 μm niobium-oxide liner to improve oxidation resistance. For both experiments the re-fabricated rod was back-filled with a binary mixture of argon (95%) and helium (5%) at 4.0 MPa. Argon was chosen to simulate the effect of low gap thermal conductivity due to fission gases. The rod plenum volume (i.e., free gas volume) was made relatively large in order to maintain stable pressure conditions until cladding burst occurred. The total free gas volume (21.5 cm^3 for IFA-650.4 and 21.5 cm^3 for IFA-650.9) was practically all located outside the heated region [54, 55].

Table 4.1: Design data of the IFA-650.4 and IFA-650.9 fuel rods [54]

	IFA-650.4	IFA-650. 9
Fuel material	UO_2	UO_2
Fuel density	95.2 %TD	95.2 %TD
^{235}U enrichment	3.5 wt%	3.25 wt%
Active fuel stack length	480 mm	480 mm
Pellet inner diameter	0 mm	0 mm
Pellet outer diameter	9.13 mm	9.13 mm
Cladding material	Zry-4 (SRA)	Zry-4 (SRA)
Cladding thickness (incl. liner)	0.725 mm	0.725 mm
Cladding outer diameter	10.75 mm	10.75 mm
Diametral gap	170 μm	170 μm
Rod inner free volume (refab.)	21.5 cm^3	19 cm^3
Rod filling gas (refab.)	Ar(95%):He(5%)	Ar(95%):He(5%)
Initial rod inner pressure (refab.)	4.0 MPa	4.0 MPa

These rodlets were located inside the IFA-650 test rig and were neutronically heated from the inside and externally heated using an electrical heater. The purpose of the heater was to simulate the effect of adjacent fuel rods within the core. The IFA-650.4 rodlet was instrumented with three thermocouples on the cladding exterior surface, a pressure transducer to measure the rod internal pressure and a cladding elongation sensor. Two of the thermocouples were located at 8 cm below the top of the fuel stack (at 180° from one another) and one was located in the plenum region 19 cm above the fuel stack. Additional temperature measurements

were provided for the coolant at the inlet and outlets of the experimental apparatus. The IFA-650.9 rodlet was also instrumented with three thermocouples on the cladding surface with one located 10 cm above the fuel bottom and two located 6.5 cm from the top of the fuel stack. A pressure transducer was also included. As with IFA-650.4, IFA-650.9 also included additional temperature measurements for the coolant at the inlet and outlets of the experimental apparatus.

Details of the Halden IFA-650 tests are well documented in [54, 55]. Each transient consists of five distinct phases: (1) preparatory (forced and natural circulation), (2) blowdown, (3) heat-up and hold at peak cladding temperature, (4) followed by scram, and (5) conclusion of the experiment. Depending upon the particular experiment, the duration and specific conditions the specimen undergoes during a phase may be different. The reader is encouraged to read the appropriate documentation for a particular analysis if interested in more specific detail.

4.2 BISON Model Settings

Since the rods analyzed in this work are used to both validate the latest developments on the HBS formation and high burnup thermal conductivity models as well as axial relocation models, BISON's `Layered1D` formulation was used to model the fuel rodlets because the axial relocation requires it in order to properly track fuel movement. In a `Layered1D` formulation, the fuel rodlet is modeled by a number of discrete axial layers. Each layer represents a single 1D generalized plane strain axisymmetric simulation. The thermo-mechanics is solved on each individual layer with global parameters such as fission gas release, internal gas volume, and plenum pressure communicated between the layers. Further details on the formulation can be found in [56]. In these analyses, 30 axial layers were used to model the fuel and cladding with one additional cladding only layer for the plenum region. Eleven `EDGE3` elements were used through the radius of the fuel and five `EDGE3` elements were used through the cladding thickness.

The base irradiation histories for the two rodlets are provided in Fig. 4.1. Both rods were subjected to seven cycles prior to re-fabrication. The thermal-hydraulic conditions for the base irradiation were not provided; therefore, typical PWR conditions were used. This includes a coolant pressure of 15.3 MPa, a coolant mass flux 3800 kg/m^2s, and an inlet temperature of 580 K.

During the experiment, the boundary conditions become extremely complex. There is the neutronic heating internally to the rod, the external heating from the heater, as well as the complicated coolant conditions due to the LOCA. The axial profile of the neutronic and electrical heater during the transient are prescribed as provided by the experimental measurements. During the preparatory phase the cladding surface temperature is prescribed based upon measurements from the thermocouples to ensure proper conditioning of the rods prior to blowdown. After blowdown the prescribed temperature is removed and the coolant transfer coefficient is significantly degraded. For the IFA-650.4 case, approximately 30 seconds after blowdown the heat transfer coefficient is set to 50 W/m^2-K and radiation between outer cladding surface and the heater is activated. For the IFA-650.9 case, the process is similar except an axial profile on the heat transfer coefficient after blowdown as suggested by [57] is employed.

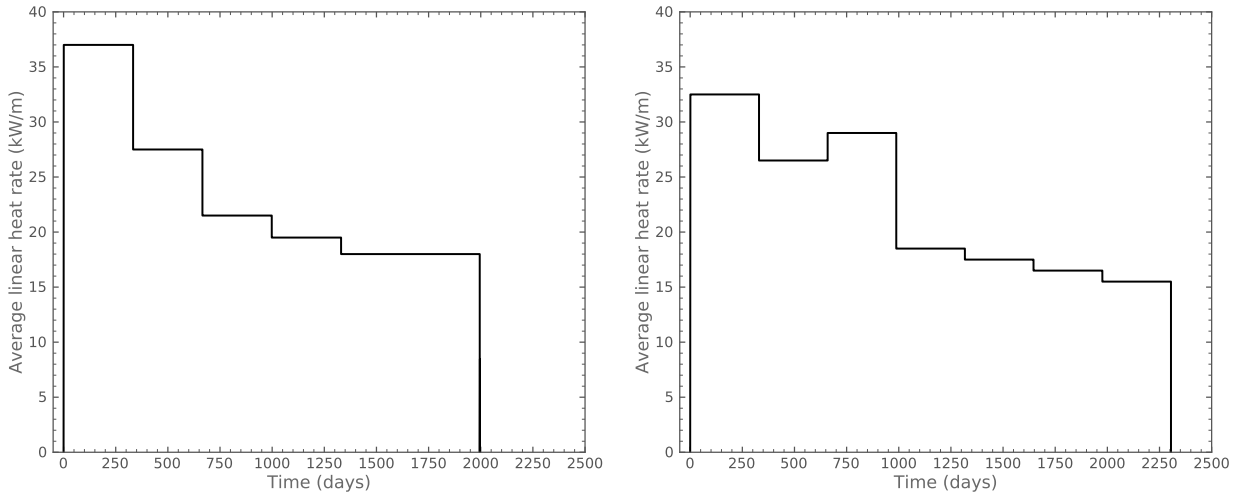

(a) IFA-650.4

(b) IFA-650.9

Figure 4.1: Base irradiation power histories for (a) IFA-650.4 and (b) IFA-650.9.

In the analyses completed here, the new HBS formation model is activated to compute the HBS volume fraction and the `STAICU` thermal conductivity model described in Chapter 2 was used with the porosity correction method proposed by `KAMPF`. The calibrated model for porosity formation (see Section 2.3) is also included. In these analyses, the BISON simulations are terminated as the time cladding rupture is predicted to occur. Cases utilizing two different failure criteria have been completed to illustrate the complexity and variability in predictions due to what is selected as the criteria for cladding rupture. The two criteria utilized in this work are [58]:

1. the *plastic instability criterion*, which deems cladding failure to occur when the inelastic strain rate exceeds $2.778 \times 10^{-2}\,\mathrm{s}^{-1}$, and
2. the *overstrain criterion*, which states that cladding failure occurs when the total inelastic strain exceeds an engineering strain value of 40%.

4.3 Results & Discussion

Comparisons between the BISON simulations and experimental measurements are provided here. The available measurements to compare against vary depending upon the experiment. All comparisons are during the LOCA transient after blowdown. For IFA-650.4, experimental measurements exist for time-to-rupture, fuel relocation, rod internal pressure, cladding elongation, and cladding surface temperature. For IFA-650.9, measurements include time-to-rupture, fuel relocation, cladding diameter, rod internal pressure, and cladding surface temperature. In this work, we focus on time-to-rupture, rod internal pressure, fuel relocation, and cladding diameter.

4.3.1 IFA-650.4

The BISON predictions are compared against the IFA-650.4 experimental data for the rod internal pressure in Fig. 4.2a, the cladding diameter in Fig. 4.2b, and the mass fraction in Fig. 4.2c. The cladding diameter is included for completeness but no experimental profilometry is available. The large single balloon observed slightly below the rodlet mid-plane corresponds to the largest accumulation of fuel as seen in Fig. 4.2c. The BISON predictions extend to a larger axial extent than the experimental specimen to ensure the total free volume within the plenum is correctly obtained. The mass fraction profile is compared against a gamma scan of the rodlet during post-irradiation examination (PIE) as varies from 0.01 to ∼2.00. A value greater than unity (i.e., >1.0) indicates the gain of mass at a particular location, whereas a value less than unity (i.e., <1.0) corresponds to mass loss. A larger concentration of gamma rays is indicative a larger mass of fuel in the region. The BISON simulations capture relocation of fuel into the large balloon; however, the length of the region devoid of fuel is different. The rod internal pressure predictions are in a good agreement with the trends following the experiment. The marker x at the end of the BISON simulation predictions indicates cladding failure. Overall, there are negligibly small differences in simulations predictions between cases with the overstrain and plastic instability failure criteria. Compared to the experimental cladding rupture time of 336.0 s, the BISON simulations predicted failure at 314.8 s and 316.5 s for the plastic instability and overstrain criteria, respectively.

4.3.2 IFA-650.9

The BISON predictions are compared against the IFA-650.9 experimental data for the rod internal pressure in Fig. 4.3a, the clad diameter in Fig. 4.3b, and the mass fraction in Fig. 4.3c. This case was analyzed previously [53]. Here, updated results are presented including the use of the HBS thermal conductivity model with porosity correction. As with IFA-650.4, the cladding profilometry predictions extend to a higher axial level than the rodlet to ensure proper computation of the internal free volume. Here, we observed a significant difference between the plastic instability and the overstrain simulations. Compared to the experimental prediction of cladding rupture at 133.0 s, the BISON simulations terminated at 136.5 s and 139.5 s for plastic instability and overstrain, respectively. The BISON simulations capture the middle balloon with reasonable accuracy and this is where rupture was predicted to occur. The large lower rupture region observed in the experiment was not captured. It is unclear based upon the thermal hydraulic boundary conditions provided how the rupture would preferentially occur at the lower region of the cladding. The mass fraction follows a similar behavior to the cladding profilometry and much more mass movement occurs for the overstrain criterion. The rod internal pressure predictions are reasonable.

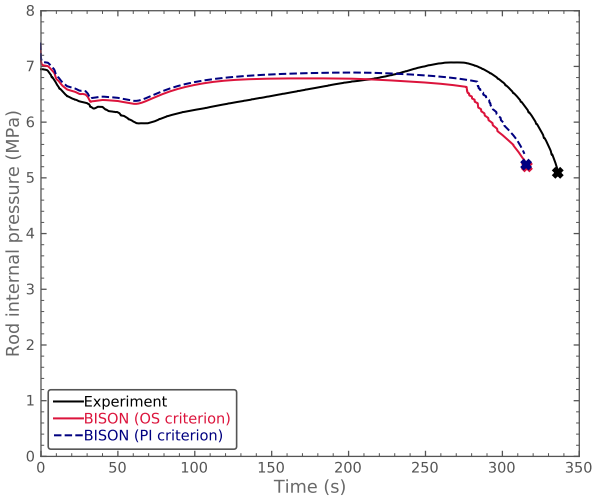

(a) Rod internal pressure

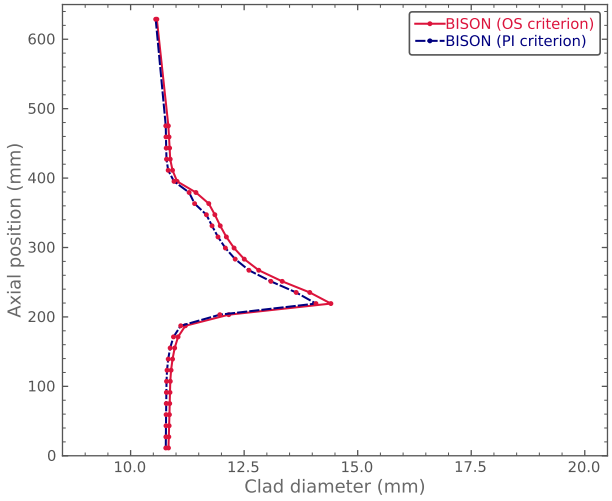

(b) Cladding diameter

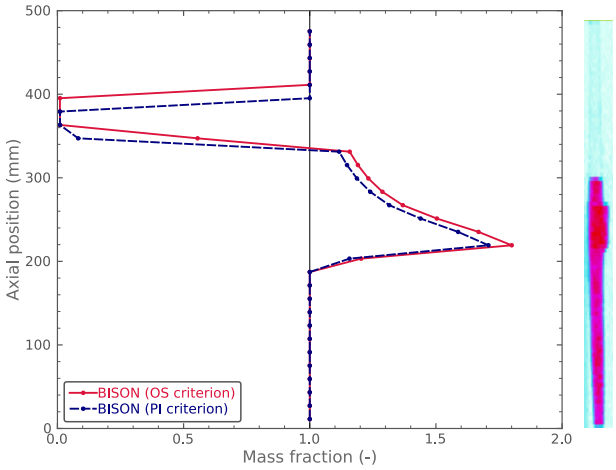

(c) Mass fraction

Figure 4.2: IFA-650.4 validation results. The cladding rupture is indicated by a 'x' marker. The plastic instability and overstrain criteria are denoted by PI and OS, respectively. The Cs-137 gamma scan is reproduced from [54].

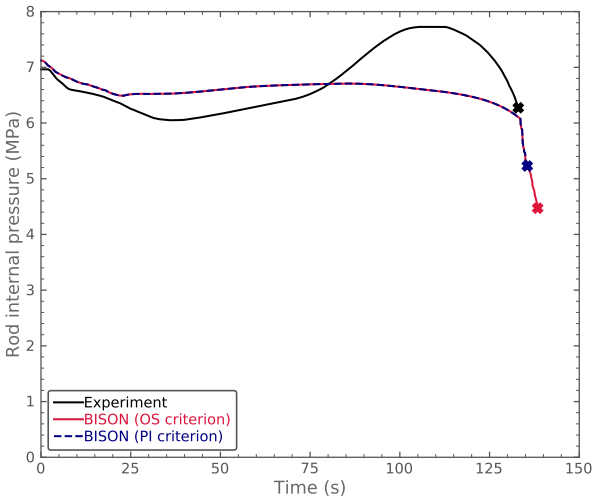

(a) Rod internal pressure

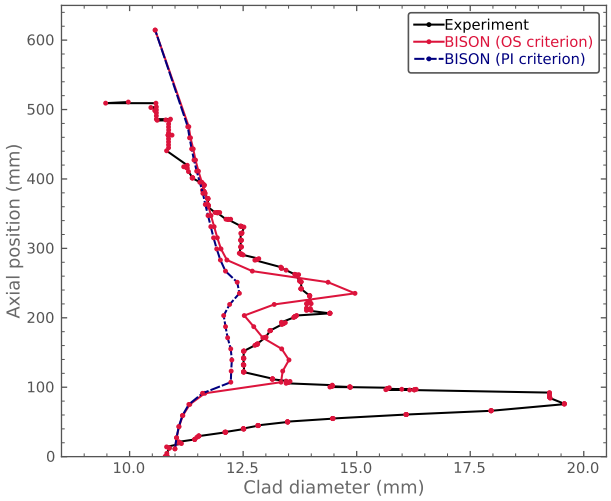

(b) Clad diameter

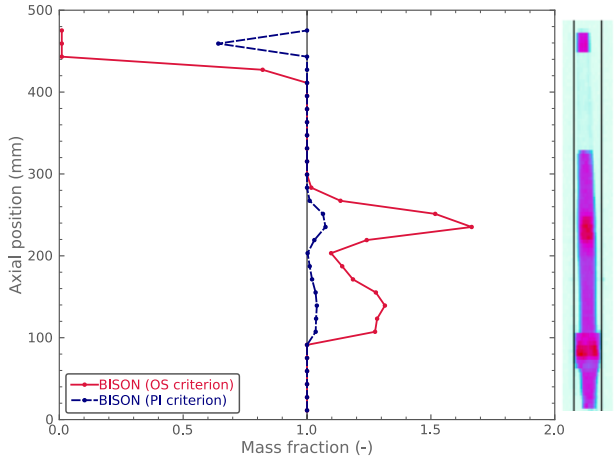

(c) Mass fraction

Figure 4.3: IFA-650.9 validation results. The cladding rupture is indicated by a 'x' marker. The plastic instability and overstrain criteria are denoted by PI and OS, respectively. The Cs-137 gamma scan is reproduced from [55].

5. Concluding Remarks

As nuclear utilities sought to extract as much energy from the fuel as possible (e.g., extending the burnup beyond $\geq 60\,\mathrm{MWd/kgU}$), new material problems arose due to increased radiation damage (e.g., high-burnup structure (HBS)), corrosion, etc. [59]. In this study, our efforts mainly focused on enhancing BISON's modeling capabilities for HBS—a complex phenomenon and an ongoing research topic in the nuclear community—to provide an improved prediction of the fuel thermal behavior at these extended burnups. The HBS modeling capabilities (see Chapter 2) that were made available in BISON are:

1. Two new thermal conductivity models for UO_2 (see Section 2.1) were implemented in BISON, which are valid up to $100\,\mathrm{MWd/kgU}$: (1) a model by Ronchi et al. [13], referred to as `RONCHI` in the `ThermalFuel` model and (2) a model by Staicu et al. [14] referred to as `STAICU` in the `ThermalFuel` model. These models account for the increase of the thermal conductivity in the region of 60–80 MWd/kgU where the HBS starts to form. This increase in the thermal conductivity is attributed to the decrease in the fission-gas concentration dissolved in the matrix during the HBS formation [18].
2. Capturing the formation of the HBS in irradiated UO_2 through BISON simulations was made possible by the implementation of the `HighBurnupStructureFormation` model (see Section 2.2). The HBS formation model allows the estimation of the local fraction of fuel that has restructured into HBS. As such, it represents a prerequisite and the basis for any future development of the code regarding HBS behavior. This BISON advancement has several implications in terms of potential future developments:
   - While in the regular UO_2 fuel structure, grains have an average size of $\sim 10\ \mu$m and tend to grow during irradiation. With HBS formation, the original grains subdivide into sub-micron grains with a size of about 0.1–0.3 μm [60, 21]. This grain refinement affects important fuel properties, such as fission-gas behavior. Future BISON development work will include modeling the evolving grain size with HBS formation and the consequences of grain refinement on fuel properties.
   - Fission-gas behavior in the HBS is substantially different from the behavior in the regular fuel structure. The sub-micrometric HBS grains undergo fission-gas depletion, and large micrometric gaseous pores form at the grain boundaries [60, 8, 21]. These pores are approximately spherical in shape and differ from the lenticular fission-gas bubbles observed at the grain boundaries of the regular fuel structure. Fission-gas pores in the HBS contribute to fuel swelling and are responsible for retention of fission gas, and for fission gas release (FGR) under certain conditions such as accidental transients [61]. A comprehensive model of fission-gas behavior in the HBS

would address both intra-granular depletion of fission gas and the evolution of grain-boundary pores, and would allow for the accurate modeling of gaseous fuel swelling and FGR at high burnup. Such a development is also of interest for the future advancement of BISON.

- Mechanical properties of the fuel, such as the elastic modulus, experience important changes with the development of the HBS [62]. It is important to account for the changes in mechanical properties with HBS formation to accurately model the mechanical behavior of high-burnup fuel. This is seen as a next step of BISON development.
- During LOCAs, the HBS tends to fragment into small pieces that can be as fine as a few tenths of microns, while the gaseous and volatile fission products retained in the HBS pores on the cracked surfaces are released. The fragments may then relocate into the ballooned region of the fuel rod and if cladding rupture occurs, they may disperse into the primary coolant. Separate-effects tests have indicated that HBS fragmentation/pulverization is caused by the increase in the pressure of the gaseous pores and the resulting stresses in the fuel [63]. Mechanistic modeling of fuel fragmentation/pulverization during LOCAs is an issue of high interest in the current context of research on nuclear fuel as it directly relates to safety and licensing issues for high-burnup fuel. Such an endeavor will require modeling the evolution of HBS gaseous pores and the development of a model for fragmentation driven by pore pressure. This is also of interest for the future development of BISON.

3. A new porosity model (see Section 2.3) was constructed based on the behavior of the experimental data from the literature [27, 28, 29] and calibrated using frequentist and Bayesian approaches. The porosity model varies as a function of local burnup and was implemented in the `ThermalFuel` model of BISON. Associated uncertainties for the model parameters and selection of the model function form were clearly provided.
4. Two new porosity correction methods (see Section 2.4) were implemented in BISON to encounter the effect of the conducting pores of HBS on the thermal conductivity. The pores were assumed to be filled with xenon and in spherical shapes for engineering purposes. Both models were made available in `ThermalFuel` model: the first method is by [30], referred to as `KAMPF` in the code, and the second method by [31, 32, 33], referred to as `LEE` in the code. The latter model is a third-order polynomial (i.e., cubic equation). A root-finding algorithm was created to obtain an analytical solution for the cubic equation. This analytical solution was validated using several different sources. Note that both correction methods are primarily based upon the heat-transfer fundamentals; therefore, they are independent of any type of fuel.

The newly implemented code capabilities are heavily dependent upon the heat-conduction equation as the underlying partial differential equation. To ensure that BISON is a faithful representation of the underlying mathematical model, a code verification study was exercised in which BISON's finite element solutions were compared to a known analytical solution as its mesh was refined. Through comparison to the expected behavior of the discretization error, it was confirmed that the numerical algorithm was behaving correctly. More exercises can be found in [44] for the verification of BISON.

After initial implementation of the code capabilities and verification of the underlying physics, it was important to investigate the actual behavior of real-world systems by performing validation activities in which the code predictions were compared to the experimental data. In this study, IFA-650.4 and IFA-650.9 rods were selected from the LOCA test series at the Halden test reactor, primarily due to the limited existing integral rod data from extended burnups. Two different cladding failure criteria (plastic instability and overstrain criteria) were used to illustrate the wide variability in LOCA modeling predictions just by selecting a different published failure criterion. Fuel relocation predictions for both rods are acceptable given the large uncertainty in the model inputs and provided boundary conditions. The simulation predictions were within 22 seconds for IFA-650.4 and within 7 seconds of the experiment for IFA-650.9.

In addition to the aforementioned HBS developments described in detail in this report, two journal publications were produced describing BISON models for UO_2 fuel and Zircaloy cladding during LOCA including separate effects and integral validation (see Chapter 6).

This work establishes a strong base for BISON's HBS modeling capabilities for UO_2 fuels at extended burnups, which can be expanded upon later. In the future, this work will be expanded to include fission-gas behavior within the HBS as well as coupling the HBS volume fraction described in Chapter 2 to other material models such as thermal conductivity porosity correction and fuel fragmentation. Additional validation cases from the Halden [51] and Studsvik [49, 50] test series will be analyzed.

6. Publications

Regarding accident capabilities in BISON, two journal publications are under revision that illustrate the LOCA model development including validation to several separate effect and integral rod analyses. Highlights of the publications are briefly provided as follows:

1. G. Pastore, R. L. Williamson, R. J. Gardner, S. R. Novascone, J. B. Tompkins, K. A. Gamble, and J. D. Hales, "Analysis of fuel rod behavior during loss-of-coolant accidents using the BISON code: Cladding modeling developments and simulation of separate-effects experiments," Journal of Nuclear Materials, 2020 (*under review*).
   Highlights:

   - Code developments for Zircaloy cladding behavior under LOCA conditions, with a primary focus on the modeling cladding high-temperature creep, crystallographic phase transition, high-temperature steam oxidation, and failure due to burst.
   - Separate-effects validation using 2D axisymmetric models for ballooning and burst behavior of Zircaloy claddings under LOCA conditions, including various temperature and inner pressure ramping rates. The measured quantities are cladding temperature, inner pressure, and time at burst failure. For example, Fig. 6.1 shows the BISON predictions of burst temperature compared to experimental data for various LOCA tests with different heating rates [64]. Note that the simulations for 10 Ks^{-1} and 30 Ks^{-1} heating rates were performed for the first time during FY20.
   - Demonstration of the cladding response in presence of azimuthal temperature variations in 3D. For example, Fig. 6.2 shows contour plots of results of a BISON 3D simulation of the REBEKA LOCA test with 1 Ks^{-1} heating rate and 10 MPa internal pressure [64], in terms of temperature, hoop strain and location where the condition for burst failure is attained. Results are shown at the time of calculated cladding burst. An azimuthal temperature variation of 30 K was considered. The 3D simulation consistently reproduces the non-uniform cladding ballooning and a localized burst on the hottest side of the cladding.

2. G. Pastore, K. A. Gamble, R. L. Williamson, S. R. Novascone, R. J. Gardner, J. D. Hales, "Analysis of fuel rod behavior during loss-of-coolant accidents using the BISON code: Fuel modeling developments and simulation of integral experiments," Journal of Nuclear Materials, 2020 (*under review*).

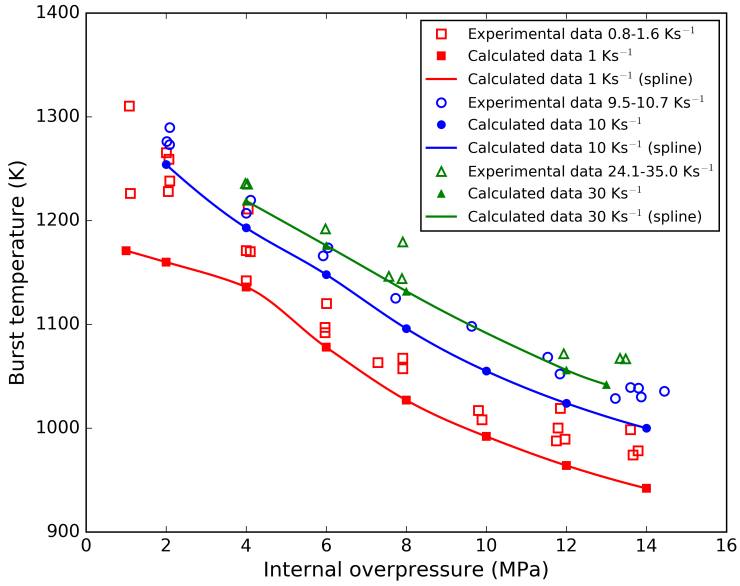

Figure 6.1: Comparison between BISON calculations and experimental data of cladding burst temperature vs. internal overpressure for the simulations of the LOCA tests REBEKA [64]. Internal overpressure is intended as the excess inner pressure relative to the outer pressure. Spline interpolations of the calculated data are also included to provide visualization of the data trend.

Highlights:

- Code developments for UO_2 fuel behavior during LOCAs, with a primary focus on the modeling axial relocation of fuel fragments during cladding ballooning.
- Integral-effects validation for three LOCA tests from the Halden IFA-650 series (e.g., IFA-650.2, IFA-650.9, and IFA-650.10), covering fresh and pre-irradiated fuel rods with and without significant axial fuel relocation. Measured quantities of fuel rod inner pressure evolution, time to cladding burst, and post-test cladding diameter profile. As an example of included results, Fig. 6.3 shows the axial profile of cladding outer diameter for IFA-650.2 at the time of simulated burst failure compared to the experimental data. A portion of each experimental profile is associated with the burst opening, which is not explicitly considered in the simulations. Two different criteria to model burst failure were applied to investigate the sensitivity of the calculated cladding strains at burst (i.e., an overstrain [strain limit] criterion and a strain rate criterion).
- Demonstration of the axial relocation of fuel fragments.

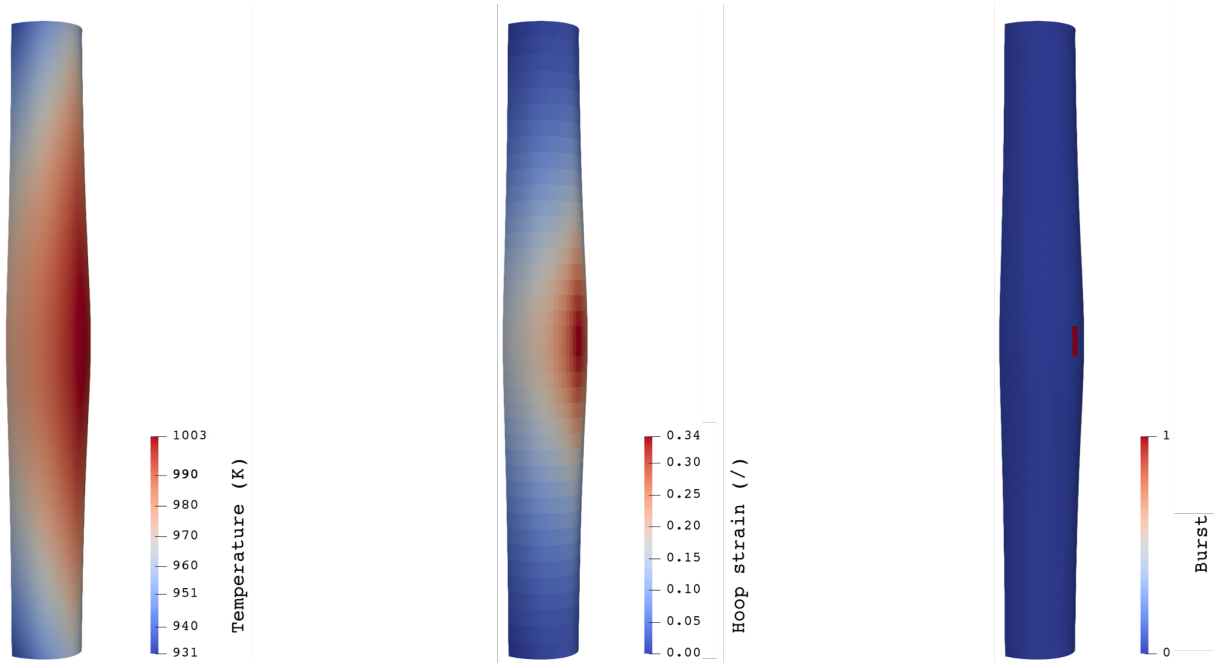

Figure 6.2: Contour plots of temperature, hoop strain and location where the burst condition is attained for the BISON 3D simulation of one of the REBEKA LOCA tests, considering a 30 K azimuthal temperature variation. The view is magnified 4 times in the radial direction for improved visualization.

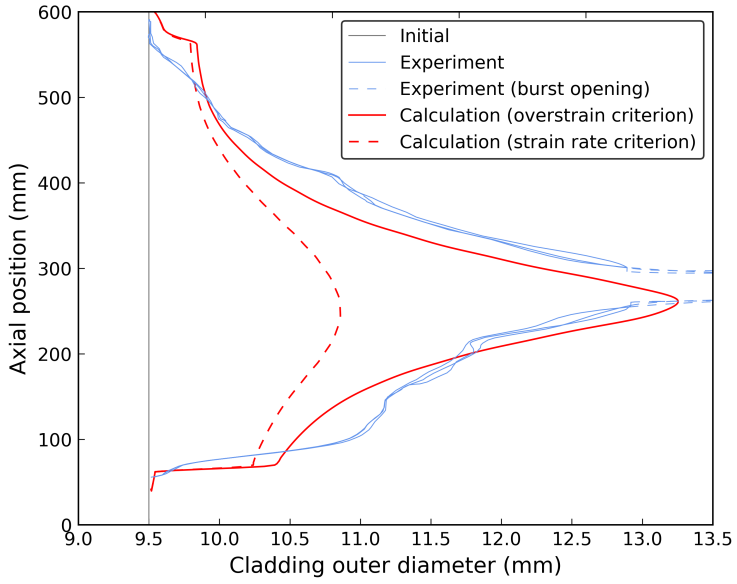

Figure 6.3: Calculated cladding outer diameter profile for IFA-650.2 at the time of simulated burst failure compared to experimental data from [65]. The three experimental profiles correspond to orientations of 0, 45, and 135 degrees with respect to the rod-rupture point.

Bibliography

[1] R. L. Williamson et al. "Multidimensional multiphysics simulation of nuclear fuel behavior". In: *Journal of Nuclear Materials* 423.1–3 (2012), pp. 149–163. DOI: 10.1016/j.jnucmat.2012.01.012.

[2] J. D. Hales et al. *BISON Theory Manual The Equations Behind Nuclear Fuel Analysis*. Idaho National Laboratory. Idaho Falls, Idaho, 2014.

[3] R. L. Williamson, J. D. Hales, et al. "BISON: A flexible code for advanced simulation of the performance of multiple nuclear fuel forms". In: *Nuclear Technology* (2020). . Manuscript submitted.

[4] D. Gaston et al. "MOOSE: A parallel computational framework for coupled systems of nonlinear equations". In: *Nuclear Engineering and Design* 239.10 (2009), pp. 1768–1778. DOI: 10.1016/j.nucengdes.2009.05.021.

[5] C. J. Permann et al. "MOOSE: Enabling massively parallel multiphysics simulation". In: *SoftwareX* 11 (2020), p. 100430. DOI: 10.1016/j.softx.2020.100430.

[6] J. D. Hales et al. "Multidimensional multiphysics simulation of TRISO particle fuel". In: *Journal of Nuclear Materials* 443 (2013), pp. 531–543. DOI: 10.1016/j.jnucmat.2013.07.070.

[7] J. D. Hales et al. *BISON TRISO Modeling Advancements and Validation to AGR-1 Data*. PEMP Notable Outcome 1.1.C Completion Report INL/EXT-20-00297. Idaho National Laboratory, July 2020.

[8] K. Lassmann et al. "Modelling the high burnup UO_2 structure in LWR fuel". In: *Journal of Nuclear Materials* 226 (1995), pp. 1–8. DOI: 10.1016/0022-3115(95)00116-6.

[9] J. Rest and G. L. Hofman. In: *Fundamental Aspects of Inert Gases in Solids*. New York: Plenum Press, 1991, p. 443.

[10] J. Rest. "Kinetics of fission-gas-bubble-nucleated void swelling of the alpha-uranium phase of irradiated U-Zr and U-Pu-Zr fuel". In: *Journal of Nuclear Materials* 207 (1993), pp. 192–204. DOI: 10.1016/0022-3115(93)90261-V.

[11] S. E. Lemekhov. In: *Int. Topical Meeting on Light Water Reactor Fuel Performance*. West Palm Beach, 1994, pp. 162–179.

[12] D. Pizzocri et al. "A semi-empirical model for the formation and depletion of the high burnup structure in UO_2". In: *Journal of Nuclear Materials* 487 (2017), pp. 23–29. URL: http://dx.doi.org/10.1016/j.jnucmat.2017.01.053.

[13] C. Ronchi et al. "Effect of burn-up on the thermal conductivity of uranium dioxide up to 100.000 MWd t^{-1}". In: *Journal of Nuclear Materials* 327.1 (Apr. 2004), pp. 58–76. DOI: 10.1016/j.jnucmat.2004.01.018.

[14] D. Staicu et al. "Effect of burn-up on the thermal conductivity of uranium–gadolinium dioxide up to 100 GWd/tHM". In: *Journal of Nuclear Materials* 453 (2014), pp. 259–268. DOI: 10.1016/j.jnucmat.2014.07.006.

[15] C. Ronchi, M. Sheindlin, and M. Musella. "Thermal conductivity of uranium dioxide up to 2900 K from simultaneous measurement of the heat capacity and thermal diffusivity". In: *Applied Physics* 85.2 (1999), p. 776. DOI: 10.1063/1.369159.

[16] R. Brandt and G. Neuer. "Thermal Conductivity and Thermal Radiation Properties of UO_2". In: *Non-Equilibrium Thermodynamics* 1.1 (1976), pp. 3–24. DOI: 10.1515/jnet.1976.1.1.3.

[17] J. K. Fink. "Review: Thermophysical properties of uranium dioxide". In: *Journal of Nuclear Materials* 279.1 (2000), pp. 1–18. DOI: 10.1016/S0022-3115(99)00273-1.

[18] D. Staicu. "2.17 - Thermal Properties of Irradiated UO_2 and MOX". In: *Comprehensive Nuclear Materials* 2 (2012), pp. 439–464. DOI: 10.1016/B978-0-08-056033-5.00038-0.

[19] W. Barney and B. Wemple. *Metallography of UO_2-Containing Fuel Elements*. Tech. rep. KAPL-1836. USA: Knolls Atomic Power Laboratory, 1958.

[20] J. Noirot, L. Desgranges, and J. Lamontagne. "Detailed characterisations of high burn-up structures in oxide fuels". In: *Journal of Nuclear Materials* 372.2–3 (2008), pp. 318–339. DOI: 10.1016/j.jnucmat.2007.04.037.

[21] V.V. Rondinella and T. Wiss. "The high burn-up structure in nuclear fuel". In: *Materials Today* 13.12 (2010), pp. 24–32. DOI: 10.1016/S1369-7021(10)70221-2.

[22] T.J. Gerczak et al. "Restructuring in high burnup UO_2 studied using modern electron microscopy". In: *Journal of Nuclear Materials* 509 (2018), pp. 245–259. DOI: 10.1016/j.jnucmat.2018.05.077.

[23] T. Barani et al. "Modeling high burnup structure in oxide fuels for application to fuel performance codes. part I: High burnup structure formation". In: *Journal of Nuclear Materials* 539 (2020), p. 152296. DOI: 10.1016/j.jnucmat.2020.152296.

[24] A.N. Kolmogorov. "On the Statistical Theory of Crystallization of Metals". In: *Ser. Mat.* 3 (1937), pp. 355–359.

[25] J. Noirot et al. "Post-irradiation examinations and high-temperature tests on undoped large-grain UO_2 discs". In: *Journal of Nuclear Materials* 462 (2015), pp. 77–84. DOI: 10.1016/j.jnucmat.2015.03.008.

[26] *BISON Code Documentation*. https://mooseframework.org/bison/syntax/bison_only_index.html.

[27] J. Spino, K. Vennix, and M. Coquerelle. "Detailed characterisation of the rim microstructure in PWR fuels in the burn-up range 40-67 GWd/tM". In: *Journal of Nuclear Materials* 231 (1996), pp. 179–190. DOI: 10.1016/0022-3115(96)00374-1.

[28] J. Spino and D. Papaioannou. "Lattice parameter changes associated with the rim-structure formation in high burn-up UO2 fuels by micro X-ray diffraction". In: *Journal of Nuclear Materials* 281 (2000), pp. 146–162. DOI: 10.1016/S0022-3115(00)00236-1.

[29] J. Spino et al. "Stereological evolution of the rim structure in PWR-fuels at prolonged irradiation: Dependencies with burn-up and temperature". In: *Journal of Nuclear Materials* 354 (2006), pp. 66–84. DOI: 10.1016/j.jnucmat.2006.02.095.

[30] H. Kämpf and G. Karsten. "Effects of Different Types of Void Volumes on the Radial Temperature Distribution of Fuel Pins". In: *Nuclear Technology* 9.3 (1970), pp. 288–300. DOI: 10.13182/NT70-A28783.

[31] B. H. Lee, Y. H. Koo, and D. S. Sohn. "Rim Characteristics and Their Effects on the Thermal Conductivity in High Burnup UO_2 Fuel". In: *Nuclear Science and Technology* 38.1 (2001), pp. 45–52. DOI: 10.1080/18811248.2001.9715006.

[32] B. Schulz. "Thermal conductivity of porous and highly porous materials". In: *High Temperatures – High Pressures* 13.6 (1981), pp. 649–660.

[33] H. Kleykamp. "Selection of materials as diluents for burning of plutonium fuels in nuclear reactors". In: *Nuclear Materials* 275 (1999), pp. 1–11. DOI: 10.1016/S0022-3115(99)00144-0.

[34] D. L. Hagrman and G. A. Reymann. *MATPRO-Version 11: a handbook of materials properties for use in the analysis of light water reactor fuel rod behavior*. Tech. rep. United States, 1979. DOI: 10.2172/6442256. URL: https://www.osti.gov/biblio/6442256/.

[35] E.W. Weisstein. *"Cubic Formula." From MathWorld–A Wolfram Web Resource*. Available at http://mathworld.wolfram.com/cubicformula.html [Online; accessed August 8, 2019].

[36] A. Toptan et al. "Modeling of gap conductance for LWR fuel rods applied in the BISON code". In: *Journal of Nuclear Science and Technology* (2020). DOI: 10.1080/00223131.2020.1740808.

[37] Guido Van Rossum and Fred L. Drake Jr. *Python reference manual*. Centrum voor Wiskunde en Informatica Amsterdam, 1995.

[38] Travis E. Oliphant. *A guide to NumPy*. Vol. 1. Trelgol Publishing USA, 2006.

[39] A. Toptan, D. J. Kropaczek, and M. N. Avramova. "On the validity of dilute gas assumption for gap conductance calculations in nuclear fuel performance codes". In: *Nuclear Eng and Design* 350 (2019), pp. 1–8. DOI: 10.1016/j.nucengdes.2019.04.042.

[40] *Wolfram—alpha widgets: cubic equation solver*. [Online; cited 2019 Dec 5]. Available at https://www.wolframalpha.com/widgets/view.jsp?id= 1beb192fcbfba3b6afa17b00ae68605a.

[41] R. L. Williamson, K. A. Gamble, D. M. Perez, et al. "Validating the BISON fuel performance code to integral LWR experiments". In: *Nuclear Engineering Design* 301 (2016), pp. 232–244. DOI: 10.1016/j.nucengdes.2016.02.020.

[42] Bison Team. *Assessment of BISON: A Nuclear Fuel Performance Analysis Code*. Tech. rep. INL/MIS-13-30314 Rev. 4. Idaho Falls, ID: INL, 2017.

[43] J. Hales et al. "Verification of the BISON Fuel Performance Code". In: *Annals of Nuclear Energy* 71 (81–90), p. 2014. DOI: 10.1016/j.anucene.2014.03.027.

[44] A. Toptan et al. *FY20 Verification of BISON using analytic and manufactured solutions*. Tech. rep. CASL-U-2020-1939-000. CASL, 2020. DOI: 10.2172/1614683.

[45] K. Salari and P. Knupp. *Code Verification by the Method of Manufactured Solutions*. Tech. rep. SAND2000-1444. Sandia National Laboratories, June 2000. DOI: 10.2172/759450. URL: https://www.osti.gov/servlets/purl/759450.

[46] D. S. Burnett. *Finite Element Analysis from Concepts to Applications*. Reading, MA: Addison-Wesley Publishing Company, 1987. Chap. 9.

[47] P. J. Scheider. *Conduction Heat Transfer*. Cambridge 42, Mass.: Addison-Wesley Publishing Company, Inc., 1955.

[48] J. C. Maxwell. *Treatise on Electricity and Magnetism*. Oxford University Press Oxford, 1873/1904.

[49] M. Flanagan and P. Askeljung. "Observations of Fuel Fragmentation, Mobility and Release in Integral High-Burnup, Fueled LOCA Tests". In: *Enlarged Halden Program Group Meeting 2011*. 2011.

[50] A. Puranen. *Post test examinations on LOCA tested rods*. Tech. rep. STUDSVIK/N-13/198. Studsvik, 2013.

[51] T. Fuketa et al. *Safety Significance of the Halden IFA-650 LOCA Test Results*. Tech. rep. NEA/C-SNI/R(2010)5. Organisation for Econocmi Co-operation and Development Nuclear Energy Agency Committeee on thte Safety of Nuclear Installations, 2010.

[52] International Atomic Energy Agency. *Fuel Modeling in Accident Conditions (FUMAC) Final: Final Report of a Coordinated Research Project*. Tech. rep. IAEA-TECDOC-1889. International Atomic Energy Agency, 2019.

[53] K. A. Gamble, R. J. Gardner, and R. L. Williamson. *BISON FY17 Accident Capability Development*. Tech. rep. CASL-U-2017-1389-000. Idaho National Laboratory, 2017.

[54] L. Kekkonen. *LOCA Testing at Halden; The Fourth Experiment IFA-650.4*. Tech. rep. HWR-838. OECD Halden Reactor Project, 2007.

[55] Bole du Chomont F. *LOCA Testing at Halden; The Ninth Experiment IFA-650.9*. Tech. rep. HWR-917. OECD Halden Reactor Project, 2009.

[56] S. A. Pitts et al. *Verify and Validate 1.5D Capability*. Tech. rep. CASL-U-2017-1380-000. Idaho National Laboratory, 2017.

[57] L. O. Jernkvist. *Computational assessment of LOCA simulation tests on high burnup fuel rods in Halden and Studsvik*. Tech. rep. 2017:12. Swedish Radiation Safety Authority, 2017.

[58] V. Di Marcello et al. "The TRANSURANUS mechanical model for large strain analysis". In: *Nuclear Engineering and Design* 276 (2014), pp. 19–29. DOI: 10.1016/j.nucengdes.2014.04.041.

[59] D. R. Olander and A. T. Motta. *Light Water Reactor Materials, Volume I: Fundamentals*. American Nuclear Society, 2017.

[60] C. T. Walker et al. "Concerning the microstructure changes that occur at the surface of UO_2 pellets on irradiation to high burnup". In: *Journal of Nuclear Materials* 188 (1992), pp. 73–79. DOI: 10.1016/0022-3115(92)90456-U.

[61] L. Holt et al. "Stand-alone modelling of the high burnup structure formation and burst release during design basis accidents". In: *Proc. of the Enlarged Halden Programme Group Meeting (EHPG)*. 2014.

[62] F. Cappia et al. "Microhardness and Young's modulus of high burn-up UO_2 fuel". In: *Journal of Nuclear Materials* 479 (2016), pp. 447–454. DOI: 10.1016/j.jnucmat.2016.07.015.

[63] K. Kulacsy. "Mechanistic model for the fragmentation of the high-burnup structure during LOCA". In: *Journal of Nuclear Materials* 466 (2015), pp. 409–416. DOI: 10.1016/j.jnucmat.2015.08.015.

[64] F. J. Erbacher et al. "Burst criterion of Zircaloy fuel claddings in a loss-of-coolant accident". In: *Zirconium in the Nuclear Industry, Fifth Conference, ASTM STP 754, D.G. Franklin Ed.* American Society for Testing and Materials. 1982, pp. 271–283.

[65] W. Wiesenack. *Summary of the Halden Reactor Project LOCA Test Series IFA-650*. Tech. rep. HPR-380. OECD Halden Reactor Project, 2013.